Wall Roughness Effects on Combustion Development in Confined Supersonic Flow

Guillaume Pelletier, Marc Ferrier, Axel Vincent-Randonnier, Vladimir Sabelnikov, Arnaud Mura

Wall Roughness Effects on Combustion Development in Confined Supersonic Flow

Guillaume Pelletier* Marc Ferrier† Axel Vincent-Randonnier‡ Vladimir Sabelnikov§
DMPE, ONERA, University of Paris Saclay, F-91123 Palaiseau, France

Arnaud Mura¶
ENSMA, 86961 Futuroscope, France

Reactive and non-reactive Reynolds-averaged Navier-Stokes (RANS) simulations of hydrogen injection into a confined transverse supersonic flow of vitiated air are conducted. The corresponding conditions were studied in the LAPCAT-II combustor. We consider two operating conditions, which differ in the value of the momentum ratio between the hydrogen and vitiated air inlet streams, thus leading to two distinct values of the equivalence ratio (ER). For its smallest value, smooth combustion develops subject to a preliminary thermal runaway period, while for its largest value, combustion is more strongly intertwined with shock wave dynamics and boundary layer separation. Special emphasis is placed on the possible effects of wall roughness on this reactive flow development. One amongst the conclusions of preliminary computational analyses of the present flowfield was that it may play a significant role on combustion development. This is firmly confirmed in the present study, which takes explicitly the influence of wall roughness into account within the equivalent sand grain modeling framework. For the largest ER value, the combustion stabilization mechanism is found to change dramatically whether roughness is taken into account or not. Its influence is assessed through a detailed comparison with available experimental data.

Keywords: Propulsion, Scramjet, Compressible flow, Turbulent flow, Wall roughness, Combustion

*Ph.D. Student, DMPE ONERA Palaiseau (France); guillaume.pelletier@onera.fr
†Research Scientist, DMPE ONERA Palaiseau (France); marc.ferrier@onera.fr
‡Research Scientist, DMPE ONERA Palaiseau (France); axel.vincent@onera.fr
§Emeritus Scientist, DMPE ONERA Palaiseau (France) and Central Aerohydrodynamic Institute (TsAGI), Moscow Region (Russia); sabelnikov@free.fr
¶Senior Scientist, Fluids, Thermal Science, and Combustion Department, Institut Pprime, UPR 3346 CNRS, ENSMA and University of Poitiers (France).

Nomenclature

Greek letters

Δu^+	velocity shift (in roughness model), $\mathrm{m\,s^{-1}}$
ε	turbulence dissipation rate, $\mathrm{m^2\,s^{-3}}$
μ	dynamic viscosity, $\mathrm{kg\,m^{-1}\,s^{-1}}$
μ_t	dynamic eddy viscosity, $\mathrm{kg\,m^{-1}\,s^{-1}}$
ν	kinematic viscosity, $\mathrm{m^2\,s^{-1}}$
ν_t	kinematic eddy viscosity, $\mathrm{m^2\,s^{-1}}$
ω	specific dissipation, $\mathrm{s^{-1}}$
$\mathbf{\Omega}$	vorticity magnitude or mean flow rate of rotation, $\mathrm{s^{-1}}$
ρ	density, $\mathrm{kg\,m^{-3}}$
τ_w	wall shear stress, $\mathrm{kg\,m^{-1}\,s^{-2}}$
$\dot{\omega}_\alpha$	production rate of the chemical species α, $\mathrm{s^{-1}}$

Roman letters

a_1	Menter's SST model constant for the calculation of ν_t, –
d	distance to the wall, m
F_2	transition functions of Menter's SST turbulence model, –
J	jet to cross flow momentum ratio ($\rho_j u_j / \rho_\infty u_\infty$), –
k	turbulent kinetic energy, $\mathrm{m^2\,s^{-2}}$
$\mathrm{k_s}$	equivalent sand grain height, m
M	Mach number, –
P	pressure, $\mathrm{kg\,m^{-1}\,s^{-2}}$
PR	ratio of total jet to static cross flow pressure ($P_{t,j}/P$)
q	mass flow rate, $\mathrm{kg\,s^{-1}}$
S_{ij}	symmetric part of the velocity gradient tensor, $\mathrm{s^{-1}}$
t	time, s
T	temperature, K
u	longitudinal velocity component, $\mathrm{m\,s^{-1}}$
u_i	velocity in direction i, $\mathrm{m\,s^{-1}}$

u_τ	friction velocity, $\mathrm{m\,s^{-1}}$
x	longitudinal coordinate, m
x_i	cartesian coordinates, m
y	wall normal coordinate, m
Y_α	mass fraction of chemical species α, –

Operators

$\overline{f}$	Reynolds average
$\widetilde{f}$	density-weighted or Favre average

Subscripts

j	relative to the jet
t	relative to total or stagnation conditions (pressure or temperature)
α	relative to species α
r	relative to rough wall
s	relative to smooth wall
s	relative to the sand grain approach

Superscripts

$^+$	non dimensional wall variable

Acronyms

BSL	BaSeLine
CFD	Computational Fluid Dynamics
CTV	Contra-rotating Trailing Vortices
CVP	Contra-rotating Vortices Pair
JISCF	Jet In Supersonic Cross-Flow
RANS	Reynolds-Averaged Navier-Stokes
SST	Shear Stress Transport (Menter turbulence model)
STV	Surface Trailing Vortices

TCI Turbulence Chemistry Interaction

I. Introduction

Several experimental test rigs have been designed and studied over the last fifty years to investigate non-premixed combustion in supersonic flows and, in many of them, hydrogen is injected into a main flow of air that can be vitiated or not. In the corresponding high temperature air flows, self-ignition conditions may be reached within the mixing layer that develops downstream of the hydrogen injection. For instance, such conditions are obtained in the coflowing jets experiments early conducted by Beach [1]. They are also met in the geometry studied by Cheng et al. [2] which consists of a supersonic burner that provides a choked main jet of hydrogen surrounded by an annular axisymmetric hot coflowing jet of vitiated air at Mach 2. Such coflowing jet geometries have been often retained as reference test cases (i.e., benchmarks) to proceed with computational studies of supersonic combustion. They have been indeed considered over the years to complete experimental databases by using advanced laser diagnostics to evaluate chemical species concentrations as well as to characterize the flowfield dynamics. Among them, the non-premixed supersonic jet flame experimentally studied by Cheng et al. [2] has been widely used as a pertaining test case for the computational modeling of supersonic turbulent combustion [3–10]. The development and stabilization of combustion downstream of a wedge or strut injector model, such as the one studied by Waidmann et al. [11, 12], has been also retained as a relevant geometry to assess the ability of computational models to describe the interaction between shock waves and hydrogen injection, which is of key importance for combustion stabilization. In this respect, the well-documented experimental database gathered by Waidmann et al. [11, 12] on a scramjet combustor model has been considered in several previous numerical investigations [13–16]. However, it should be fairly acknowledged that the operative conditions associated to these various Laboratory setups remain rather far from those operated in scramjet prototypes. On the one hand, the stagnation temperature levels reached in the wedge injector experiments conducted by Waidmann et al. [11, 12] remain too moderate to trigger some typical effects of supersonic combustion conditions and, on the other hand, the development of free coflowing jets in the atmosphere is not representative of the large scale mixing phenomena taking place in the more realistic geometry of wall injection into a confined high-enthalpy airstream.

Other experiments were therefore developed to study high-speed mixing and combustion in a simple

scramjet-like engine environment. For instance, a direct-connect supersonic combustor model, often referred to as the SCHOLAR experiment, has been presented in reference [17]. The model consists of a copper section (approximately 550 mm in length) followed by a longer carbon steel section attached to the aft end of the copper section. The copper section contains an inclined single injector that delivers hydrogen into a vitiated airstream [17]. Other reference datasets have been obtained within the framework of the international research programs. The objective was to demonstrate the feasibility of igniting and maintaining supersonic combustion under realistic flight conditions. On the one hand, flight tests have been performed. A scramjet model was accelerated up to Mach 8 with a rocket and, between the altitudes of 23 km and 35 km, hydrogen was injected into the scramjet and pressure variations were sampled. A flight Mach number between seven and eight has been recorded. On the other hand, ground tests have been carried out at different conditions in the T4 shock tunnel facility [18] and in a high-enthalpy shock tunnel [19] so as to obtain correlations with flight-based tests. Scramjet-like engine environment experiments have been also performed on the LAPCAT-II geometry. The LAPCAT-II combustor is fed with a hot vitiated airstream at Mach 2 issued from a Laval nozzle. This vitiated airstream results from a preliminary H_2-air combustion and O_2 replenishment so as to maintain the molar fraction of O_2 at 0.21. Stagnation temperature levels can be as high as $1800 - 1900$ K while the stagnation pressure levels can reach 1.0-1.2 MPa. This facility is operated in the blow-down mode with the test section working as a heat-sink. The overall length of the combustor is around 1260 mm and it is equipped with large optical accesses to proceed with either single-point measurements or imaging techniques. Its geometry features a constant width of 40 mm and consists of four successive sections: the first one has a constant cross-section with an inlet height of 35.4 mm while, to prevent thermal choking, the following three sections are characterized by a one-degree (318 mm long), a three-degree (354.5 mm long), and finally a one-degree (305 mm long) diverging half angles, respectively. The outlet of the combustor is connected to a 400 mm diameter exhaust pipe where the pressure level is around 0.1 MPa so that the non-reactive flow is overexpanded at the combustor exit. A more detailed description of the experimental setup and conditions will be provided in the next section. At this level, it should be emphasized that the structural integrity of the device is ensured through a thermal protection coating and the corresponding coating leads to a significant level of wall roughness.

In the conditions that were investigated, flow visualizations highlighted two combustion regimes depending on the equivalence ratio [20, 21]. In this respect, it should be emphasized that, in contrast to transverse injection in free (i.e., open) conditions, the present geometry is relevant to combustion developement in a

scramjet combustor and, for the corresponding confined flow conditions, the equivalence ratio (ER) quantifies two distinct fuel injection effects which may favor the occurence of thermal choking within the combustor: the first one is the added mass and the second one is the heat release induced by chemical reactions. This explains why the ER is preferred to any other quantities (including the J-number) so as to parameterize the different cases. In the first regime (ER = 0.121), after a rather long induction length (thermal runaway processes), which reflects the large values of the ignition delay of the reactive mixture, the pressure gradually increases in the combustor, while the flowfield remains mostly supersonic. This specific regime will be hereafter denoted as the *supersonic smooth (or weak) combustion regime.* This is in contrast to the second regime (ER = 0.145) where ignition takes place earlier and stabilization occurs through a stronger interaction process between combustion and aerodynamics (i.e., shock waves and boundary layer separation), thus giving rise to a sharp increase of the wall pressure. The resulting flowfield features large subsonic regions, which are relevant to thermal choking, i.e., choked or partially choked conditions. This regime will be hereafter denoted as the *sudden or sharp (partially choked) combustion regime.*

Previous numerical studies of the LAPCAT-II combustor [20, 22] have shown that wall roughness may have a significant impact on the combustion development and that its consideration should lead to a better agreement with experimental data. Since wall roughness increases skin friction, its influence was mimicked, in these studies, by artificially and arbitrarily increasing the molecular viscosity coefficient, the influence of which is restricted to the viscous sub-layer with the other parts of the flow remaining dominated by turbulent mixing. One amongst the conclusions of these previous works was that it would be more satisfactory to address the description of roughness effects by using a systematic methodology based on effective roughness measurements. At this level, it seems worth emphasizing that some smooth wall computations were also performed for various values of the turbulent Schmidt number. From a practical point of view, the corresponding set of computations was found unable to reproduce the change of behavior that is observed in the experiments, i.e., the change of flow topology obtained in case B (ER=0.145) vs. case A (ER=0.121), whereas it was found possible through the consideration of the roughness model.

The effects of wall roughness can be evaluated using three distinct methods [23]. The first strategy makes use of either direct numerical simulations (DNS) or large-eddy simulations (LES) and computes the flow around the roughness elements. It is quite clear that its application is restricted to simplified situations as the corresponding computational costs become prohibitive for complex geometries. This is in contrast to the discrete element approach where the mean flowfield transport equations are spatially averaged over

roughness elements, which allows to take into account the roughness blockage effect. Since it requires some case-dependent modifications of the transport equations, this technique however cannot be systematically implemented in RANS computational fluid dynamics (CFD) solvers. Finally, because of its relative simplicity with respect to the two previous strategies, the so-called equivalent sand grain approach remains the most popular for engineering purposes. The objective with such a methodology is to reproduce the skin friction increase that is induced by wall roughness. The skin friction increase can indeed be related to a shift downwards of the logarithmic region of the boundary layer profile [24]. In this respect, many correlations have been proposed in the literature to evaluate this velocity shift as a function of a quantity suited to represent the roughness, namely the equivalent sand grain height k_s [24–26]. Finally, it is also noteworthy that, within the RANS framework, several authors proposed to modify the wall boundary conditions of the turbulence models so as to reproduce the skin friction increase or, equivalently, the velocity shift [23, 27–30].

The objective of the present work is to assess the possible influence of wall roughness on the numerical simulation of supersonic combustion in conditions relevant to the LAPCAT-II experiments. In contrast to the previous works of Vincent-Randonnier et al. [20] and Balland et al. [22], we used a systematic methodology, which is based on effective roughness measurements. It makes use of the modeling proposal of Aupoix et al. [23], which relies on the equivalent sand grain approach. The study focuses on the global analysis of combustion stabilization and development in conditions relevant to the two combustion modes mentioned above. The characterization of the unsteadiness of the reactive flowfield is not the primary objective of the present study and RANS simulations are therefore preferred to LES. In this respect, it should be emphasized that the consideration of wall roughness effects within the LES framework still remains quite challenging [31]. The manuscript is organized as follows: after a brief presentation of the experimental set-up and main tests results in Section II, the third section provides the salient features of the computational model with some emphasis placed on the description of wall roughness modeling. Finally, the obtained computational results are gathered in Section IV which includes a systematic comparison between results obtained either with or without any account of wall roughness effects into the simulations. The two modes of combustion that were highlighted from experiments are considered and possible mechanisms through which wall roughness can modify the reactive flow topology and combustion stabilization are proposed and discussed. Finally, the manuscript ends with a conclusion section where some perspectives for future works are set forth.

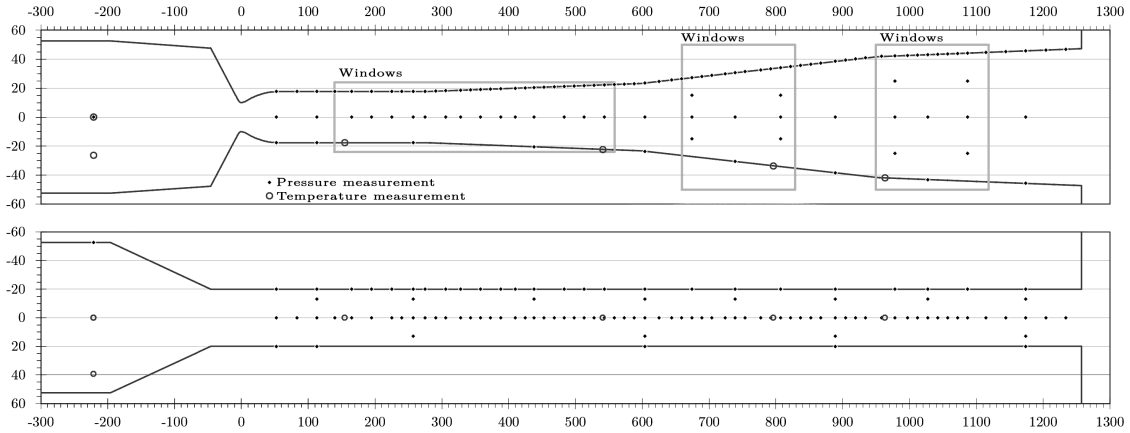

Figure 1 General schematic of the LAERTE facility

II. Brief presentation of the experimental data

The LAERTE facility is equipped with the LAPCAT-II dual mode scramjet combustor since 2010, see Fig. 1 and 2. The scramjet model is fed with a hot vitiated airstream, which is generated by the preliminary combustion of a H_2-air mixture followed by O_2 replenishment so as to keep the value of the oxygen molar fraction equal to 0.21. The inlet stagnation temperature can be varied within the range 1300-1900 K with a stagnation pressure between 0.1 and 1.2 MPa. The facility is operated in the blow-down mode with the test section working as a heat-sink. The overall duration of one single test is around seventy seconds but its useful duration, i.e., at the required level of temperature, lasts over approximately seven seconds, depending on the operative conditions that is considered.

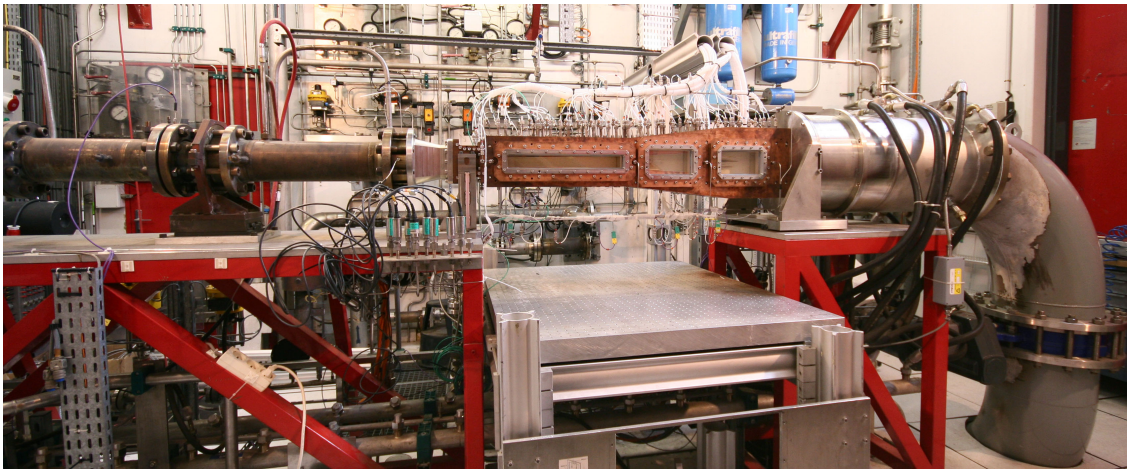

Figure 2 View of the LAPCAT-II supersonic combustor integrated with the LAERTE facility

During the experiments, the pressure profile along the combustor is recorded by using up to 128 wall

pressure transducers, which are sampled at a frequency of 10 Hz. The values of the stagnation pressure P_t and temperature T_t are deduced from measurements performed 220 mm upstream from the throat of a Laval nozzle in a pipe featuring an inner diameter of 105 mm. At this location, the Mach number value is sufficiently small to approximate P_t from the recorded wall pressure and the stagnation temperature is obtained from thermocouple measurements.

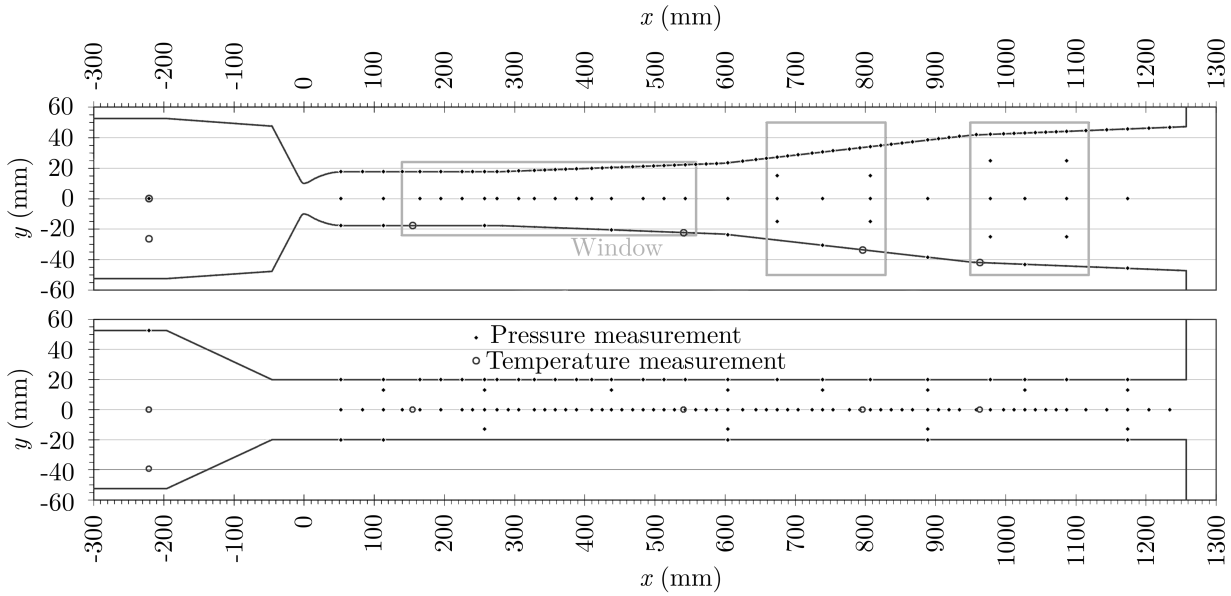

Figure 3 Geometry of the LAPCAT-II combustor equipped with optical accesses and pressure probes, side view (top) and top view (bottom).

A. The LAERTE facility and the LAPCAT-II supersonic combustor

The combustor features a constant width of 40 mm and consists of four successive sections. The first section — isolator — has a constant cross-area with an inlet height of 35.4 mm. Its length is 215 mm. It is followed by three additional sections, which are characterized by a one-degree (318 mm length), a three-degree (354.5 mm length), and again a one-degree (305 mm length) diverging half angles in order to prevent thermal choking. The total length of the combustor, including the spacing between the nozzle exit and the isolator inlet, is 1257 mm. It features large optical accesses, which allow optical diagnostics to be settled; this includes single-point measurements techniques (CARS, LIF or DLAS) or imaging techniques (shadowgraphy or Schlieren, PLIF, high-speed imaging). The Laval nozzle is used to generate the supersonic flow entering the combustor. Figure 3 depicts the profile of the Mach 2 Laval nozzle together with the combustor geometry and locations of pressure sensors. The reference position $x = 0$ mm corresponds to the throat of the nozzle.

The outlet of the combustor is connected to a 400 mm diameter exhaust pipe where the pressure remains approximately constant and equal to 0.1 MPa. The combustion chamber is made of a copper alloy and its inner walls include a 300 μm thick thermal barrier coating (TBC) made of Yttria-stabilized Zirconia (Yttria denotes Yttrium oxyde). The TBC surface resembles sandpaper and has been characterized using scanning electron microscopy (SEM), showing an average characteristic roughness size of around 65 μm.

The set of computations presented in the next sections corresponds to experiments conducted with the combustor fueled with pure hydrogen. The sonic injection of hydrogen into the main supersonic flow of vitiated air is operated through two holes (2 mm diameter) located at x = 200 mm in the middle of the top and bottom walls of the test section. Fuel pressure and temperature are measured 104 mm upstream from the corresponding injection point. Four thermocouples are used to evaluate the temperature of the lower wall of the combustor at x = 155 mm, x = 541 mm, x = 796 mm, and x = 963 mm, with the thermal barrier coating overlaying the wall and thermocouples.

B. High-speed Schlieren and OH* imaging

The compressible and reactive flow structure has been characterized thanks to high-speed Schlieren imaging technique coupled to OH* radical chemiluminescence imaging. The Schlieren images have been acquired at a frequency of 12 kHz with an exposure time of 1 μs, which induces a motion blur resulting from a flow motion up to 1.5 mm during the exposure time. The Schlieren imaging field corresponds to a 43 mm $\times$ 96 mm area. The OH* images have been acquired with an ultraviolet-intensified high-speed camera at a frequency of 4 kHz with an exposure time of 4 μs. The OH* emission signal is selected using a narrowband filter, which is characterized by a maximum transmission at around 310 nm and a 10 nm full width at half maximum. The OH* imaging field corresponds to a 50 mm $\times$ 100 mm area. A beam splitter has been used to superimpose the fields associated to Schlieren and OH* imaging, and the camera trigger signals have been synchronized.

Table 1 Experimental conditions

	P_t (bar)	T_t (K)	Y_{N_2}	Y_{O_2}	Y_{H_2O}	q (g/s)	$P_{t,j}$ (bar)	$T_{t,j}$ (K)	PR	J	Φ
case A	4.03	1704	0.5775	0.2554	0.1671	290.1	3.91	305	7.59	1.0	0.121
case B	4.07	1706	0.5852	0.2476	0.1672	291.7	4.78	300	9.19	1.2	0.145

The present study is focused on the consideration of two distinct runs: 20151123-R10 and 20151123-R09, hereafter denoted as cases A and B, the conditions of which are gathered in Table 1. In this table, quantities with the subscript j are related to the hydrogen injection, while the other quantities are related to the flow

issued from the Laval nozzle, i.e., the main vitiated airstream. The last three quantities, on the right, are the ratio of the jet stagnation pressure and the main flow static pressure (i.e., PR = $P_{t,j}/P$), the jet to vitiated airstream momentum ratio $J = (P_j\,\gamma_j\,\mathrm{M}_j^2)/(P\,\gamma\,\mathrm{M}^2)$, and the equivalence ratio Φ. In the expression of the J-number, the quantities P, γ, and M correspond to the static pressure, the ratio of specific heats, and the Mach number, respectively.

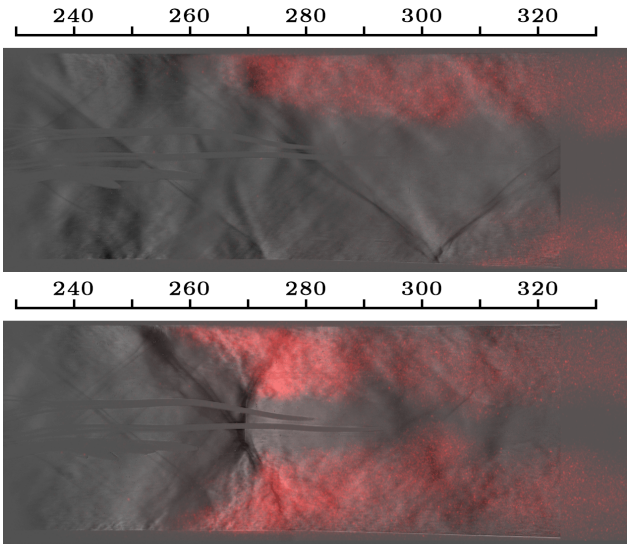

Figure 4 OH* visualization superimposed on Schlieren image for cases A (top) and B (bottom), with x-abscissa provided in mm on the top of each figure.

The momentum ratio J is larger for case B, as is the associated global equivalence ratio Φ. Experiments show that case B is characterized by the presence of a high pressure peak while, for case A, the wall pressure record increases more smoothly (i.e., progressively) with the longitudinal coordinate. Figure 4 displays snapshots of OH* emission superimposed on the Schlieren image for the two runs. It has to be recalled that the hydrogen injection port is located at abscissa x = 200 mm downstream of the nozzle throat, so that the hydrogen jet cannot be seen in these figures. Horizontal ridges (or ribs), which are visible in the center of the duct for x-abscissa smaller than 280 mm, correspond to dirt accumulation on the optical access. Figure 5 reports longitudinal pressure profiles, taken in the plane of symmetry, along the upper wall. After a pressure increase associated to combustion development for x-abscissa larger than 200 mm, followed by a decrease and a plateau, the pressure level decreases again in the second diverging section, which is the sign of supersonic

flow conditions. Finally, at the end of this second section, there is a large pressure rise, which indicates that the combustor is not entirely started.

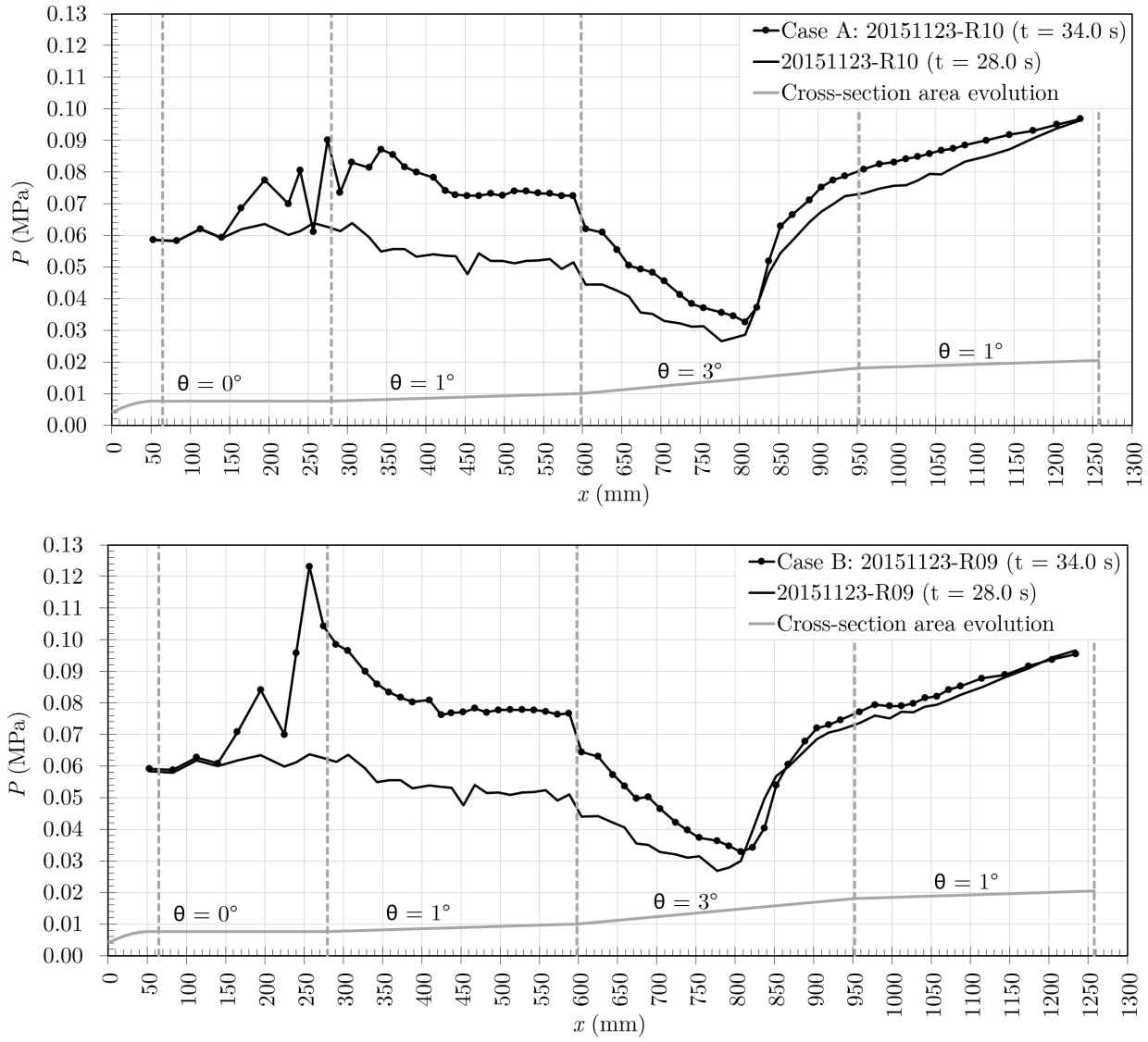

Figure 5 Longitudinal profiles of the static pressure for case A (top) and case B (bottom), with x-abscissa provided in mm on the bottom of each figure.

Considering the Schlieren image of case A, which is reported in Fig. 4, it puts into evidence the succession of oblique shock-waves and turbulent activity in the vicinity of walls, which is more clearly visible on the lower wall before combustion develops, i.e., for x-abscissa smaller than 300 mm. In reference [20], Vincent-Randonnier and his coworkers studied the same configuration for similar conditions but with a visualization window that was shifted slightly upstream, in such a manner that the hydrogen injection is visible. In this respect, the figure numbered 13 in reference [20] suggests that (i) the shock structure mentioned above may

result from the wall reflection of the bow shock generated by the transverse hydrogen jet, and (ii) the turbulent structures from the corresponding wake and the associated turbulent mixing region, see also references [32, 33] for further details. Taking a closer look at the OH^* emission, it can be seen that combustion takes place rather far downstream of the hydrogen injection at abscissa larger than 260 mm for the upper wall, and at abscissa larger than 300 mm for the lower wall. Thus, the upper and lower stabilization zones are not established at the same location. The combustion dynamic, which remains to be analyzed in further details, shows that the corresponding zones are asymmetric on the top and bottom walls, they move back and forth. In the corresponding region, the mean pressure profiles exhibit some small pressure peaks relevant to supersonic flow conditions. From these observations, it is concluded that case A corresponds to a rather standard mode of combustion in supersonic flow: after injection, the fuel inlet stream mixes with the vitiated airstream and, after a preliminary thermal runaway period, ignition takes place with a combustion development that does not markedly alter the high-speed flowfield, which remains mostly supersonic. Therefore, this case will be referred to as *the supersonic weak combustion mode*.

The topology of the reactive flow, as well as the pressure profiles, are substantially different for case B. Indeed, for this higher equivalence ratio, combustion stabilization takes place further upstream and coincides with the birth of a cross-shaped shock structure, see Fig. 4. Experimental data show that the stabilization region and the cross-shaped shock structure move together, thus reflecting the strong intertwinment that exists between the shock-induced compression effects and the initiation of chemical reactions. At this location, the visible height of the turbulent structures seems to be quite larger than in the other case, thus suggesting the occurence of significant boundary layer separation. These observations support the following mechanism of combustion stabilization: at this larger equivalence ratio, the combustion-induced pressure gradient is larger and leads to boundary layer separation and to the formation of the cross-shaped shock structure. These two phenomena favor combustion stabilization since they generate subsonic regions featuring reduced velocities and higher temperatures. Since it is related to the birth of large subsonic regions, which are characteristic of situations close to thermal choking, this case will be hereafter referred to as the *sudden or sharp (partially choked) combustion mode*. Finally, it is noteworthy that, for higher equivalence ratio, pressure starts to rise upstream of the hydrogen injection and the corresponding regime was previously considered in reference [20].

III. Computational model

A. Description of the numerical solver

The present numerical study has been conducted with the ONERA computational fluid dynamics code CEDRE [34]. CEDRE is a multi-physics platform that relies on several specific solvers to handle complex flow simulations including multi-component reacting flows, radiating flows, two-phase flows featuring a dispersed phase within either an Eulerian or a Lagrangian framework, films and heat conduction in solids, etc. In the present work, only the CHARME solver, that deals with reacting flows, is used. This solver is extensively used for simulating supersonic combustion at ONERA [35]. It is a three-dimensional compressible and reactive Navier-Stokes solver that relies on a finite-volume (FV) framework applied to either structured or unstructured computational meshes. The numerical treatment of inviscid fluxes makes use of the HLLC (Harten-Lax-van Leer Contact) approximate Riemann solver [36]. Second-order accuracy is achieved via variable extrapolation, i.e., monotonic upwind scheme for conservation laws (MUSCL) [37]. It is applied in conjunction with Van Leer flux limiters to ensure monotonicity [38]. The viscous fluxes are evaluated with a second-order centered scheme. The CEDRE solver has been extensively verified using classical numerical benchmarks including Sod shock tube, Poiseuille and Taylor flowfields, etc. As far as computational validation is concerned, the implemented models for two-phase flows, combustion, and turbulence have been also extensively validated, and assessed through many previous investigations such as those conducted by Chedevergne et al. [39, 40], Dorey et al. [41], Sainte-Rose et al. [42], Doisneau et al. [43], or Moule et al. [8, 44].

The set of governing equations corresponds to the compressible form of the reactive Navier-Stokes equations. It includes balance equations for mass, chemical species mass fractions, momentum and energy, and it describes convection, molecular diffusion and chemical reaction processes. The considered flowfield is turbulent. Since the classical Reynolds averaging introduces many additional unknown correlations associated with density fluctuations, a mass-weighted Favre averaging is preferred, so that the mean value of any quantity Φ is defined by $\widetilde{\Phi} = \overline{\rho\Phi}/\overline{\rho}$, with $\Phi'' = \Phi - \widetilde{\Phi}$ the associated fluctuation,

$$\frac{\partial \overline{\rho}}{\partial t} + \frac{\partial}{\partial x_j}\left(\overline{\rho}\,\widetilde{u}_j\right) = 0 \tag{1}$$

$$\frac{\partial}{\partial t}\left(\overline{\rho}\,\widetilde{Y}_\alpha\right) + \frac{\partial}{\partial x_j}\left(\overline{\rho}\,\widetilde{u}_j\widetilde{Y}_\alpha\right) = \frac{\partial}{\partial x_j}\left(-\overline{\rho u_j'' Y_\alpha''} - \overline{J}_j^{Y_\alpha}\right) + \overline{\dot{\omega}}_\alpha \tag{2}$$

$$\frac{\partial}{\partial t}\left(\overline{\rho}\,\widetilde{u}_i\right) + \frac{\partial}{\partial x_j}\left(\overline{\rho}\,\widetilde{u}_j\,\widetilde{u}_i\right) = \frac{\partial}{\partial x_j}\left(-\overline{\rho u_j'' u_i''} - \overline{P}\,\delta_{ij} + \overline{\tau}_{ij}\right) \tag{3}$$

$$\frac{\partial}{\partial t}\left(\overline{\rho}\,\widetilde{e}_t\right) + \frac{\partial}{\partial x_j}\left(\overline{\rho}\,\widetilde{u}_j\,\widetilde{e}_t\right) = \frac{\partial}{\partial x_j}\left(-\overline{\rho u_j'' e_t''} - \overline{J}_j^{e_t} + \widetilde{\sigma}_{ij}\widetilde{u}_i\right) \tag{4}$$

where ρ denotes the density, u_j is the j-component of the velocity field, Y_α is the mass fraction of chemical species α, $J_j^{Y_\alpha}$ is the j-component of the molecular diffusion flux for the chemical species α, with $\alpha = 1, \ldots, n_s$ (n_s being the total number of chemical species), $\dot{\omega}_\alpha$ is the species production (or consumption) rate, τ_{ij} is a component of the viscous stress tensor. The species molecular viscosity is evaluated from the Sutherland law [45] and the resulting viscosity μ of the mixture is computed from a weighted average based on the species mass fractions, i.e., $\mu = \sum_{\alpha=1}^{\alpha=n_s} Y_\alpha \mu_\alpha$. In the above expression, P denotes the pressure, $e_t = h - P/\rho + u_i u_i/2$ is the total energy per unit mass, and finally $J_j^{e_t}$ is the j-component of the total energy molecular flux. We assume Fourier heat conduction, with a thermal conductivity deduced from the Eucken model, and Fickian molecular diffusion. The molecular diffusivity coefficient of any chemical species, i.e., D_α, is deduced from the ratio of the viscosity μ and a constant Schmidt number Sc_α. It is noteworthy that the present set of computations is conducted with Schmidt number values set to unity. The specific heat of chemical species are determined from a seventh-order polynomial $c_{p,\alpha}(T) = \sum_{k=0}^{k=7} a_{k,\alpha} \left(T/T_s\right)^k$, where T_s is a scaling factor used to compute the coefficients a_k according to NASA and NIST-JANAF thermochemical tables.

Reynolds-averaged Navier-Stokes numerical simulations are performed within the Menter's k-ω shear stress transport (SST) framework [46] with the Reynolds fluxes of mass and energy, i.e., $\overline{\rho u_j'' Y_\alpha''}$ and $\overline{\rho u_j'' e_t''}$, deduced from the turbulent diffusivity approximation by introducing turbulent Schmidt and Prandtl numbers, which are set to a standard value of 0.9 [47]. The k-ω SST model was designed to give an improved prediction of the onset and amount of flow separation under adverse pressure gradients. Its performance has been illustrated in a large number of validation studies [48].

Thus, based on reference [49], the turbulent flowfield is determined from the following two transport equations

$$\frac{\partial \overline{\rho} k}{\partial t} + \frac{\partial}{\partial x_j}\left(\overline{\rho}\,\widetilde{u}_j k\right) = \frac{\partial}{\partial x_j}\left(\left(\mu + \sigma_k \mu_t\right)\frac{\partial k}{\partial x_j}\right) + P_k - \beta^* \overline{\rho}\, k\, \omega \tag{5}$$

$$\frac{\partial \overline{\rho} \omega}{\partial t} + \frac{\partial}{\partial x_j}\left(\overline{\rho}\,\widetilde{u}_j \omega\right) = \frac{\partial}{\partial x_j}\left(\left(\mu + \sigma_\omega \mu_t\right)\frac{\partial \omega}{\partial x_j}\right) + P_\omega - \beta \overline{\rho}\, \omega^2 + 2\overline{\rho}\left(1 - F_1\right)\sigma_{\omega_2}\frac{1}{\omega}\frac{\partial k}{\partial x_i}\frac{\partial \omega}{\partial x_i} \tag{6}$$

where the production terms are defined as follows

$$P_k = \max\left[\min\left(-\overline{\rho u_i'' u_j''}\frac{\partial \widetilde{u}_i}{\partial x_j}; 20.0\overline{\rho}\beta^*\, k\,\omega\right); 0\right] \tag{7}$$

$$P_\omega = \left(\overline{\rho}\,\gamma/\mu_t\right) P_k \tag{8}$$

with $\beta^* = 0.09$. The other modeling constants present in Eq. (5), (6), and (8) are evaluated from the following general expression $\zeta = F_1\,\zeta_1 + (1 - F_1)\,\zeta_2$, where ζ denotes σ_k, σ_ω, β or γ, while the quantity F_1 corresponds to a blending function

$$F_1 = \tanh\left(\eta_1{}^4\right) \text{ with } \eta_1 = \min\left[\max\left(\frac{\sqrt{k}}{\beta^*\omega y}; \frac{500.0\nu}{y^2\omega}\right); \frac{4.0\rho\sigma_{\omega_2}}{\mathrm{CD}_{k\omega}y^2}\right] \tag{9}$$

with

$$\mathrm{CD}_{k\omega} = \max\left(2\overline{\rho}\sigma_{\omega_2}\frac{1}{\omega}\frac{\partial k}{\partial x_i}\frac{\partial \omega}{\partial x_i}, 10^{-20}\right) \tag{10}$$

The two sets of coefficients values involved in the blending operation are $\sigma_{k_1} = 0.85$, $\sigma_{\omega_1} = 0.5$, $\beta_1 = 0.0750$, $\gamma_1 = \beta_1/\beta^* - \sigma_{\omega_1}\kappa^2/\sqrt{\beta^*}$, and $\sigma_{k_2} = 1.0$, $\sigma_{\omega_2} = 0.856$, $\beta_2 = 0.0828$, $\gamma_2 = \beta_2/\beta^* - \sigma_{\omega_2}\kappa^2/\sqrt{\beta^*}$, with $\kappa = 0.41$, respectively.

The SST representation differs from Menter's baseline model (BSL) in the addition of a SST limiter in the definition of the turbulent viscosity:

$$\nu_t = \frac{a_1 k}{\max(a_1\omega; \mathbf{\Omega}\mathrm{F}_2)} \tag{11}$$

where $\omega = \varepsilon/k$ with k the turbulent kinetic energy and ε its dissipation rate, and with the value of ω determining the characteristic length scale of turbulence. In the original version of the SST model [46], hereafter denoted as BSL model, the quantity $\mathbf{\Omega}$, which is involved in Eq. (11), was associated to the norm of the antisymmetric part of the mean velocity gradient tensor (i.e., the modulus of the mean flow rotation rate) whereas, following reference [49], it denotes herein its symmetric part, i.e., the mean flow strain rate. The value of the modeling constant a_1 that appears in Eq. (11) is $a_1 = 0.31$ [23] and the blending function F_2 is defined by $\mathrm{F}_2 = \tanh\left(\eta_2{}^2\right)$, with the non-dimensional parameter η_2 determined from

$$\eta_2 = \max\left(\frac{2.0\,\sqrt{k}}{\beta^*\,\omega\,y}; \frac{500.0\,C_\mu\,\nu}{\omega\,y^2}\right) \tag{12}$$

where ν denotes the molecular viscosity and y is the distance to the wall. This correction to the BSL model is aimed at avoiding the overestimation of the turbulent viscosity in shear layers. However, as emphasized in the next sections, it may interfere with the representation of the wall roughness. The details of the corresponding wall roughness modeling will be provided in section III.E.

Further details about the turbulent reactive flow modeling will be provided in the next sections of the

manuscript. Finally, while the time evolution from the initial conditions to the final state is effectively computed, it is worth emphasizing that steady-state RANS solutions are seeked and, as a consequence, the temporal accuracy is not an issue. Therefore, the temporal integration is performed by using a simple first-order numerical scheme. For the present set of computations, temporal integration is performed with a time step set equal to 10^{-6}s using this first-order implicit numerical scheme until steady-state conditions are reached: the mass flow rates between the inlets and the outlets are balanced and wall pressure is steady.

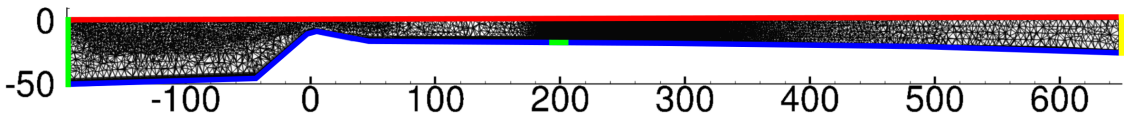

Figure 6 Computational domain retained to perform the numerical simulation of the LAPCAT-II combustion chamber. Boundaries conditions are delineated in color.

B. Computational geometry

The computational domain is restricted to 195 mm before the throat of the Mach 2 Laval nozzle up to 650 mm downstream of its location, so that only the started part of the combustor is simulated. The computational cost is reduced by considering only half of the combustion chamber geometry. The computational mesh retained to perform the numerical simulation of the LAPCAT-II combustor is composed of prism layers along the walls and tetrahedrons in the rest of the flow, see Fig. 6. In this figure, the green boundaries correspond to inlet boundary conditions. At the vitiated airstream inlet (on the left), stagnation pressure and temperature are imposed while the velocity is adjusted to enforce the mass flow rate that is determined from the choked nozzle condition. At the bottom, the hydrogen injector is modelled as a surface corresponding to its diameter, where sonic inlet Dirichlet boundary conditions are applied. No-slip boundary conditions are applied on the walls (blue color in Fig. 6), while the red color corresponds to a symmetry condition. Values at the exit of the computational domain (yellow color) are determined from extrapolation rules since, as it will be seen later on, this corresponds to a supersonic outlet.

Table 2 Details of the computational mesh

x (mm)	-195.0< x <65.0	65.0< x <198.0	198.0< x <201.0	201.0< x <300.0	300.0< x <650.0
Δ (mm)	1.5	2.0	0.15	0.4	0.4 to 4.0
h (10^{-3}mm)	3.0	2.0	1.0	3.0	2.0

The whole computational mesh features approximately 8,500,000 cells. It is refined at the fuel injector inlet and downstream in order to obtain a satisfactory description of the mixing layer. The computational resolution is linearly derefined further downstream so as to reduce computational costs. The main characteristics of the resulting computational mesh are gathered in Table 2. In this table, the quantity Δ denotes the characteristic size of the computational cell, while h is the height of first prism layer, i.e., in the direct vicinity of the wall. All dimensions are provided in millimeters. The dimensions of the computational cells in the direct vicinity of the wall have been chosen in such a manner that the dimensionless wall distance $Y^+ = h\,u_\tau/\nu$, with u_τ the friction velocity, remains of the order of unity. The corresponding distributions, i.e., probability density function and cumulative density function, are reported in Fig. 7. Finally, it should be emphasized that, in the computational results section IV, the numerical visualizations are mirrored with respect to the (x,z) plane, in order to make easier the comparison with experimental visualizations.

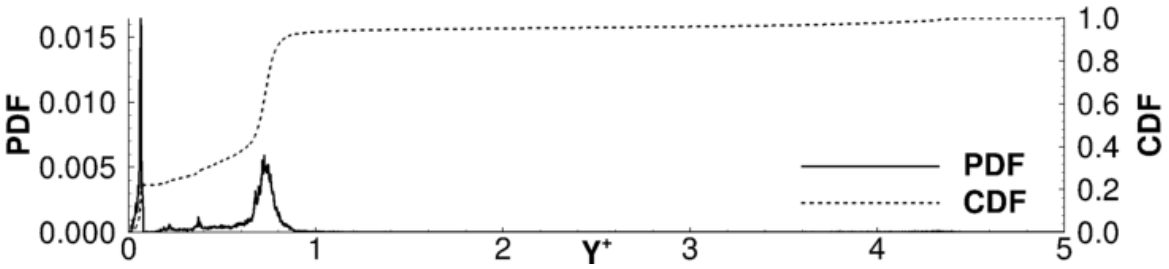

Figure 7 Cumulative and probability density functions of the dimensionless wall distance Y^+.

C. Grid sensitivity analysis

Four different meshes are created with STAR-CCM$^+$ to study the influence of the grid refinement on the computational results. The total numbers of cells for each geometry are provided in Table 3. All meshes are composed of tetrahedral cells and prism layers alongside the walls. The mesh is refined in the vicinity of the hydrogen injection, where the characteristic cell size has been decreased. Computations of the supersonic weak combustion mode are conducted using a smooth wall boundary condition for each mesh M_1, M_2, M_3, and M_4.

Table 3 Mesh characteristics

	M_1	M_2	M_3	M_4
Number of cells	2 256 887	4 656 263	8 888 199	15 830 828

In a first step of the analysis, we proceed with a standard grid convergence analysis retaining the solution obtained on the most refined mesh (i.e., M_4) as a reference. In this respect, it should be emphasized that such standard analyses of truncation errors are very useful for structured (regular) grids because, on sequences of refined meshes, the truncation errors converge as $\mathcal{O}(h^p)$, with h is a characteristic mesh size and p the order of accuracy of the computational method [50, 51]. The corresponding analysis is conducted on the pressure field. Thus, to assess the evolution of numerical errors, the results obtained on mesh M_4 are used as a reference solution and the L_2-norm is retained as the relevant metric of the numerical errors:

$$\mathcal{E}_2^{M_h} = \sqrt{\frac{1}{n_h}\sum_{i=1}^{i=n_h}\left(P_i^{M_h} - P_i^{M_4}\right)^2}, \tag{13}$$

where n_h denotes the total number of cells of mesh M_h.

The error decay rate is depicted in Fig. 8. It displays a slope that lies between unity and two. However, for unstructured grid computations such as those reported herein, it is known that the convergence of standard truncation errors may be misleading and such an analysis requires the use of windowing together with consistent refinment strategies [52], which lie outside the scope of the present work. Therefore, the present grid sensitivity analysis is concluded with a more practical inspection of the evolution of the wall pressure distribution in the symmetry plane as the computational mesh is refined.

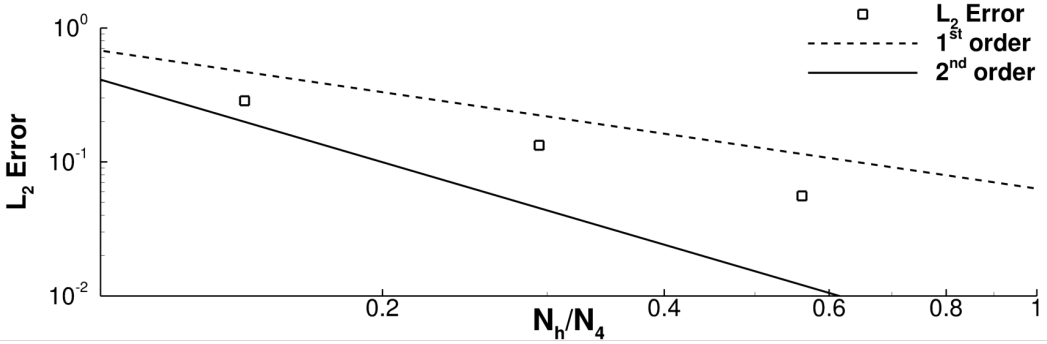

Figure 8 Error decay rates based on the L_2-norm of the pressure error computed for different meshes.

The corresponding longitudinal profiles of static pressure obtained for each mesh, see Fig. 9, show that, for the coarser mesh (Mesh 1), both the flow upstream of the injection and the ignition zone are only poorly reproduced. The three other meshes exhibit rather similar results in the combustion zone ($x > 300.0$) but meshes M_3 and M_4 lead to a better description of the pressure evolution (i) upstream of the injection (bow shock) and (ii) in the diverging sections for abscissa larger than x = 400.0. Considering this set of

computational results, mesh M_3 has been retained as a satisfactory compromise for the numerical analysis of the present geometry.

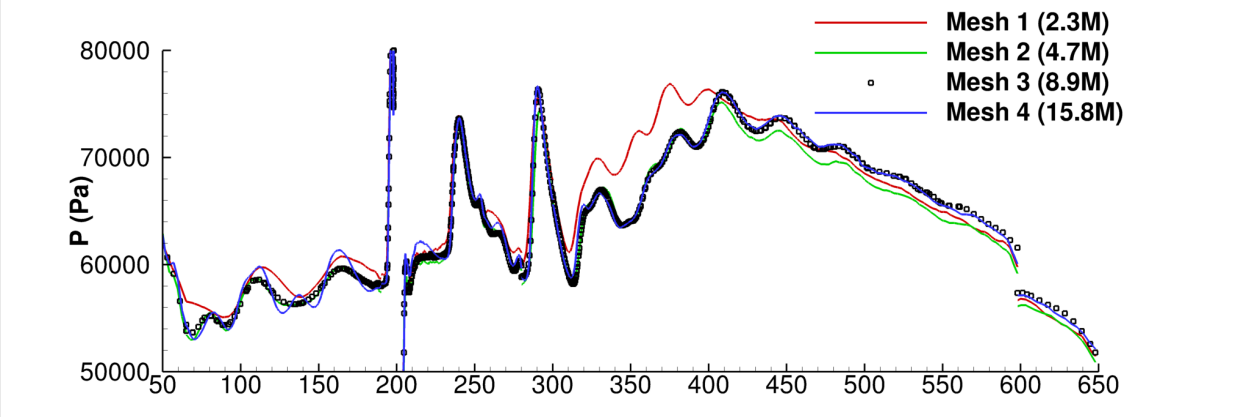

Figure 9 Wall pressure profiles comparison in the plane of symmetry for differents meshes.

D. Turbulent reactive flow modeling

As emphasized above, the closure of the Reynolds-averaged Navier-Stokes transport equations is obtained within the framework of the two-equation k-ω Menter's shear stress transport (SST) model [46]. The averaged chemical production rates $\overline{\dot{\omega}}_\alpha$ that appear in the averaged species mass fraction transport equations, see Eq. (2), are represented within the quasi-laminar or well-stirred reactor (WSR) framework. This quasi-laminar or perfectly stirred reactor (PSR) approximation consists in neglecting the possible influence of unresolved fluctuations of composition at the resolved level. In this framework, the averaged or filtered reaction rates are evaluated directly from the detailed chemical scheme applied to the resolved composition: $\overline{\dot{\omega}}_\alpha = \dot{\omega}_\alpha \left(\widetilde{T}, \widetilde{Y}_\alpha \right)$. In this respect, it must be emphasized that such a PSR or well-stirred reactor (WSR) representation is standardly retained as a one of the elementary building blocks of supersonic combustion modeling within either the RANS or the LES framework [53–56]. The composition of the reactive mixture of hydrogen and vitiated air is described using nine chemical species: H_2, H_2O, N_2, O_2, OH, H, O, HO_2 and H_2O_2, and the finite-rate chemical reactions are described with the eighteen step chemical scheme proposed by Jachimowski [57]. In this respect, it seems worth emphasizing that, for the present conditions, turbulent combustion is indeed expected to be chemistry-controlled, especially for the smallest value of the momentum ratio J, which is associated to a smooth (or weak) combustion development subject to a preliminary thermal runaway period. Based on standard estimates, the values of the Damköhler number obtained for the present conditions are indeed smaller than unity. Finally, it should also be recalled that, as underlined in the introduction of the manuscript,

combustion is here mainly influenced by wall roughness, and the representation of turbulence-chemistry interactions (TCI) seems to be less important for the purpose of the present study.

E. Modeling of the roughness effects

As emphasized in the introduction, the equivalent sand grain approach is retained to take wall roughness into account [23]. In this framework, the first step of the methodology consists in determining the equivalent sand grain size, hereafter denoted k_s, which is, for a given experiment, the characteristic size of sand grains that would lead to the same drag increase as the one observed in Nikuradse's experiments [24]. It is indeed worth recalling that, in Nikuradse's experiments, the wall roughness increase is obtained by using a dense deposit of sand grains. In the present study, the observed roughness, which is associated to the thermal barrier coating (TBC), is considered to be equivalent to a sand grain deposit, the mean characteristic height of which has been evaluated to be equal to 65 μm using SEM. This value will be retained as the equivalent sand grain height in the following. The second step of the methodology consists in introducing this value into a model able to reproduce the drag increase induced by this roughness. In his early work [24], Nikuradse pointed out that the corresponding drag increase can be related to a downward shift, in the logarithmic region, of the profile of the mean longitudinal velocity component. Several models have been introduced in the literature so as to relate this velocity shift and the equivalent sand grain size k_s. These models are expressed in terms of dimensionless quantities written with respect to wall quantities: $k_s^+ = k_s u_\tau/\nu$, $u^+ = u/u_\tau$, and $y^+ = y u_\tau/\nu$, where $u_\tau = \sqrt{\tau_w/\rho}$ denotes the friction velocity based on the wall shear stress. Among these dimensionless quantities, the normalized roughness factor k_s^+ appears as a key parameter, which compares the characteristic height of the protrusions, or equivalent grain size, with the thickness of the laminar sublayer. As long as it remains smaller than unity, the protrusions remain confined within the laminar viscous sublayer and one may expect that the wall could still be considered as hydraulically smooth. In this respect, it should be emphasized that this ratio k_s^+ can also be thought as a Reynolds number that is formed by the equivalent sand grain size k_s and friction velocity u_τ.

Several strategies have been proposed to reproduce the velocity shift Δu^+ in turbulence closures [23]. For instance, in his two-equation k-ω model [27], Wilcox adds a correction on the specific dissipation ω so that it tends towards a finite value at the wall. The resulting decrease leads to an enhanced turbulence compared to a smooth wall, and thus to higher skin friction levels. Aupoix [23] found that this correction leads to satisfactory results for sufficiently large roughness levels ($k_s^+ > 10$) but tends to overestimate the velocity shift Δu^+ for smaller values. Willcox thus proposed an additional correction to fix this issue [28] but

it was subsequently found to lead to unrealistic results within the transition region. However, once applied to the SST model, the Willcox's correction produces a velocity shift that is dramatically underestimated for values of k_s^+ larger than thirty, see reference [23] for further details. This can be readily explained from the expression of the SST limiter, as given by Eq. (11). The use of the Willcox's correction indeed decreases the dissipation rate close to the wall, compared to the smooth wall case that activates the SST limiter thus hindering the increase of the turbulent kinetic energy. Therefore, Hellstein and Laine [29] proposed to modify the expression of the SST limiter by multiplying the term ΩF_2 present in Eq. (11) by a function F_3, which aims at restricting the effects of the limiter to the logarithmic zone, thus discarding its influence close to the wall. The behaviour of this correction remains satisfactory as long as k_s^+ remains smaller than one thousand but, for larger roughness levels, it is found to underestimate the velocity shift [23]. Finally, following the work of Aupoix and Spalart [58], Knopp et al. [30] proposed to modify not only ω, as suggested by Willcox, but also to impose a non-zero finite value to the turbulent kinetic energy k and this strategy leads to quite satisfactory results except in the transition region [23].

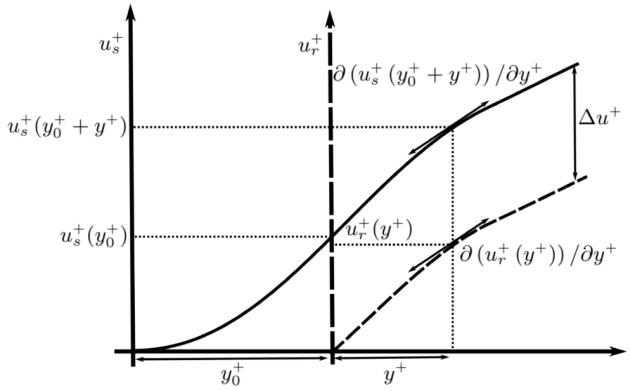

Figure 10 Illustration of the velocity shift procedure

In the vicinity of the wall, there is a region of the flow, called the roughness sublayer, which is highly perturbed by the presence of the roughness elements. Above this region, the main flow characteristics, once scaled by the increased friction level, are expected to retain some similarities with those developping over smooth surfaces in such a manner that the logarithmic law is preserved but shifted. The velocity shift approach thus consists in deducing the velocity derivative in rough wall conditions from a velocity shift applied to the normalized velocity profile associated to smooth wall conditions. This may be illustrated by

considering two distinct frames of reference with one related to the rough wall flowfield and the other related to the smooth wall flowfield. The corresponding longitudinal components of the velocity are denoted u_r^+ and u_s^+ for the rough and smooth walls, respectively, and the principle of the method is schematically depicted in Fig. 10.

From a practical viewpoint, the velocity shift is determined from the velocity profile obtained along a smooth wall with the condition that it corresponds to the same flow resistance, i.e., the same velocity gradient, as the one obtained along the rough wall:

$$\frac{\partial}{\partial y^+}\left(u_r^+(y^+)\right) = \frac{\partial}{\partial y^+}\left(u_s^+(y^+ + y_0^+)\right) \tag{14}$$

where y_0^+ denotes the shift that is applied when changing from the rough-wall towards the smooth-wall frame of reference. Once integrated, this leads to $u_r^+(y^+) = u_s^+(y^+ + y_0^+) - u_s^+(y_0^+)$, a relation from which the velocity shift is readily deduced:

$$\Delta u^+ = u_s^+(y^+ + y_0^+) - u_r^+(y^+) = u_s^+(y_0^+) \tag{15}$$

which shows that the velocity shift is equal to the velocity obtained at a distance y_0^+ from a smooth wall. In this respect, it is noteworthy that the dimensionless momentum equation in the near wall region reads $(1 + \nu_t^+)(\partial u^+/\partial y^+) = 1$, which implies that the shift of coordinate applies to the turbulent viscosity [23]. It also applies to the normalized turbulent kinetic energy and frequency, in such a manner that one may write $k_r^+(y^+) = k_s^+(y^+ + y_0^+)$ and $\omega_r^+(y^+) = \omega_s^+(y^+ + y_0^+)$. Models giving the altitude y_0^+ at which the velocity magnitude on smooth wall is equal to the velocity shift Δu^+ in Eq. (15) can be determined for reference solutions and can be established for each turbulence closure [23]. Finally, for rough-wall conditions, finite values are imposed at the wall for the turbulent kinetic energy and specific dissipation, and, for the SST model, which is presently retained as the turbulence closure, the corresponding expressions for $k(y = 0) = k_w = k_w^+ \cdot u_\tau^2 = k_s^+(y_0^+) \cdot u_\tau^2$ and $\omega(y = 0) = \omega_w = \omega_w^+ \cdot u_\tau^2/\nu = \omega_s^+(y_0^+) \cdot u_\tau^2/\nu$ can be found in reference [23].

IV. Analysis of computational results

Numerical simulations of the LAPCAT-II combustor have been previously performed for various operating points, including conditions close to those studied herein. For instance, Vincent-Randonnier *et al.* [20] carried out RANS simulations with CEDRE for $P_t = 0.4$ bar, $T_t = 1614$ K and $\Phi = 0.1$. These computations were also performed with the Menter's SST model used in conjunction with a quasi-laminar approach based

on the Jachimowsky chemical scheme to describe hydrogen-air combustion [57]. For the corresponding operating conditions, the experimental pressure distribution is quite similar to the one observed for the present auto-ignition case. The authors investigated the possible influence of wall temperature and wall roughness on the ignition process, and found that the best agreement with experiments is obtained only if wall roughness effects are taken into account. Since no roughness model was available in CEDRE at this time, the possible effects of roughness on flow resistance was mimicked by increasing the molecular viscosity coefficient. The argument was that such a modification would have an effect that is restricted to the viscous sublayer, with the rest of the flow remaining dominated by turbulent mixing. An increase of the molecular viscosity by a factor of four was found necessary to reproduce satisfactorily the experimental pressure level and distribution.

Balland and Vincent-Randonnier [22] performed RANS simulations for conditions P_t = 0.4 bar, T_t = 1350 K and Φ = 0.15 using the same solver and modeling ingredients as those retained in reference [20]. For this lower stagnation temperature, combustion is observed to take place farther downstream, in a large separated zone that develops in the second diverging section of the combustor. Roughness effects are investigated by using the same methodology as the one described above, i.e., through a modification of the molecular viscosity coefficient. Since combustion takes place in a region featuring low velocity and high temperature levels, the effects of wall roughness remains rather weak. However, the authors concluded that its consideration increases the pressure level upstream of the ignition zone, which leads to a slightly improved level of agreement with experiments. This is a direct consequence of the wall roughness that induces a thickening of the boundary layer. This effect can be important for the development of combustion within a confined environment, as it will be shown below in section IV.B.2. It is also worth noting that, for these two studies, (i) a significant effect of wall temperature has been pointed out and (ii) experimental pressure profiles have been recovered numerically only through the consideration of wall temperature BC values larger than those issued from experiments.

Finally, Fureby and his coworkers [21] recently performed LES simulations for three distinct conditions. The first one is related to a combustion mode taking place in the recirculation zone while, for the two others, the conditions are such that P_t = 0.4 bar, T_t = 1505 K, Φ = 0.15 and P_t = 0.4 bar, T_t = 1697 K, Φ = 0.15. On the one hand, for the first set of conditions, according to pressure distribution profile reported in reference [21], the combustion development seems to be quite similar to the present supersonic weak combustion mode mode. On the other hand, the second set of conditions is very similar to those associated to the present

partially choked combustion mode, and the corresponding pressure profiles indeed display some similarities. The simulations reported in reference [21] are also based on the quasi-laminar chemistry approach but the computations make use of another chemical mechanism to describe hydrogen-air combustion. In contrast to the present study, no particular wall treatment is used. For these two cases, the level of agreement with experimental pressure profiles is satisfactory, but the authors noticed that, in comparison with experimental results, numerical simulations lead to an earlier combustion development. For the second set of conditions, combustion even occurs in the small recirculation zone that develops upstream of hydrogen injection whereas any trace of OH^* has been detected in this area during experimental campaigns.

To conclude, the possible influence of wall roughness effects on the development of combustion in the LAPCAT-II combustor has been highlighted in some recent studies [20, 22]. In these studies, the possible influence of an increased flow resistance that can be induced by wall roughness has been modeled through an artificial increase of the molecular viscosity. It should be recognized that it would be quite more satisfactory to account for the influence of wall roughness on the flowfield by resorting to an effective roughness measurement and a generic modeling procedure. This is the methodology that will be followed in the next sections of this manuscript, using the framework described in section III.E and the roughness height measurements performed with SEM, see section II.A. In the following section, the possible influence of roughness on the non-reactive flow topology is first analyzed through a comparison with the data available from the literature. Then, in section IV.B, the corresponding effects are evaluated by comparing numerical and experimental results obtained in reactive cases for both the weak combustion and the sudden (partially choked) combustion modes. Mechanisms through which wall roughness may influence the combustion development are also discussed.

A. Brief description of the non-reactive flowfield

In this section, we consider the non-reactive flowfield that develops in the direct vicinity of the transverse injection of hydrogen in the supersonic vitiated airstream. This corresponds to the well-known jet in supersonic cross-flow (JISCF) topology. However, in contrast to most of the numerical simulations reported in the literature, the present set of computations takes the wall roughness into account using the model described in section III.E. Such a compressible flowfield topology has been extensively described in the literature, e.g. [32, 33]. Its main features are depicted in Fig. 11 and Fig. 12. The jet first expands in the supersonic crossflow at x = 200 mm. It is then re-compressed through a barrel shock that ends with a Mach disk. The barrel shock acts as a blunt body blockage that leads to the formation of a bow shock in the supersonic vitiated airstream. The barrel shock is folded and a highly sheared layer develops between the bow shock and

the barrel shock.

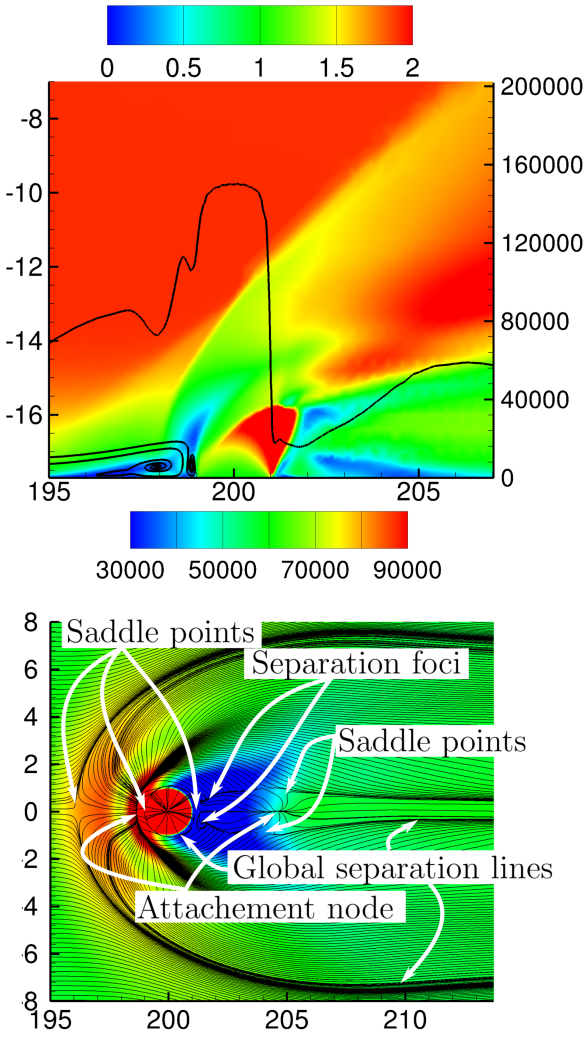

Figure 11 Mach number contours together with pressure profile and streamlines in the plane of symmetry (top). Pressure contours together with streamlines in the (y = 0.1 mm)-plane (bottom).

Besides this typical compressible flow pattern, the JISCF exhibits a rather complex vortical structure. In addition to the well-known jet counter-rotating trailing vortices (CTV) [32, 33, 59, 60] — also often referred to as the counter-rotating vortices pair (CVP) — there are several other near-wall vortex structures that can be inferred from the skin friction streamlines reported in Fig. 11. As the vitiated airstream approaches the jet, the boundary layer separates leading to the formation of a horseshoe vortex, as identified by the blue

volumic streamlines in Fig. 12. The associated separation line is visible on the right side of Fig. 11. The formation of this vortex is accompanied by a separation shock associated to a pressure increase, which is followed by a pressure decrease in the vicinity of the vortex core. A secondary counter-rotating vortex is also visible at the upstream foot of the barrel shock. Close to the symmetry plane, this secondary vortex is delineated by an attachment line, which is shared with the horseshoe vortex, and a second separation line. The later goes around the injection hole since the secondary vortex is trapped by the low pressure region behind the barrel shock. The secondary vortex is identified by the red volumic streamlines in Fig. 12 and it appears to be the main contributor to the CTV.

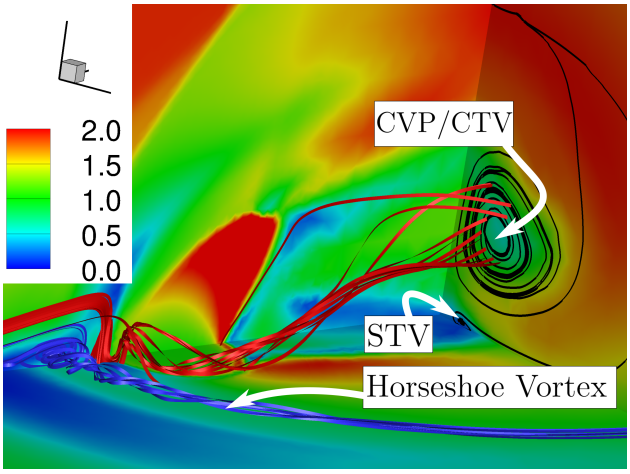

Figure 12 Topology of the JISCF as depicted using the Mach number contours, volumic streamlines, and surface streamlines in a transverse plane.

In reference [59], Lu and Dickmann discussed the flow topology of the JISCF configuration, in terms of skin friction lines similar to those reported at the bottom of Fig. 11, for a very large range of pressure ratio PR. From a qualitative viewpoint, the present flow topology, which corresponds to a value PR = 7.6, is quite similar to the one reported in the work of Lu and Dickmann for PR = 15.0: it displays two foci of separation, two saddle points, an attachment node, and two lines of separation. These two lines are the wall imprint of two vortices, which are often denoted surface trailing vortices (STV), see for instance [32]. Finally, as a preliminary conclusion, it can be stated that the presence of roughness does not seem to alter significantly the global topology of the non-reactive JISCF.

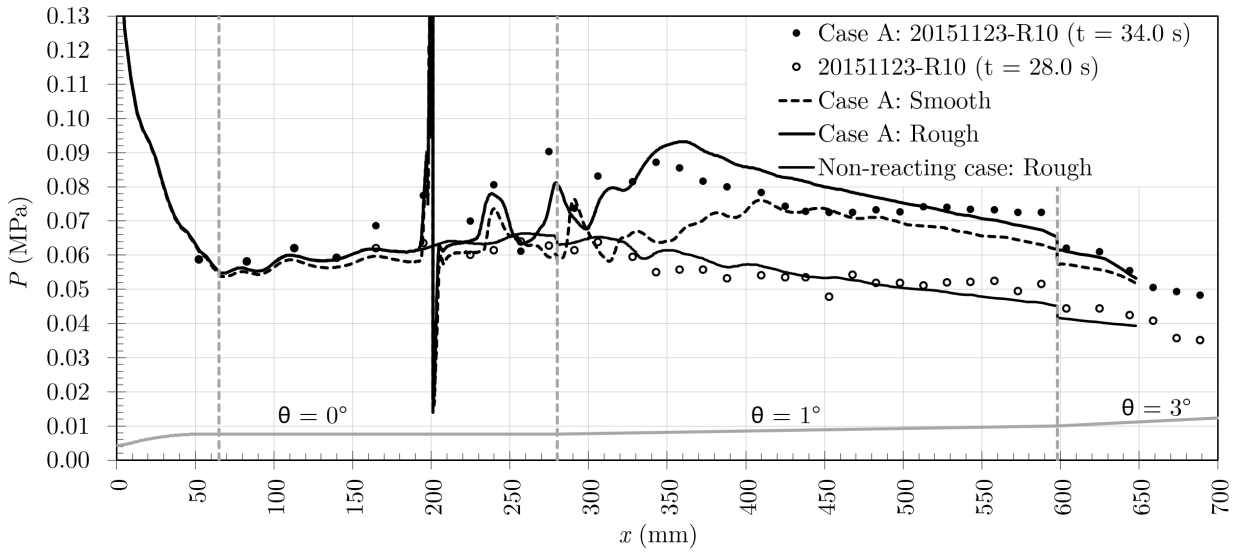

Figure 13 Wall pressure profiles comparison in the plane of symmetry.

B. Reactive flow analysis

1. Supersonic weak combustion mode

In this section, simulations results are compared to experimental data for the *supersonic weak combustion mode*, hereafter referred to as case A, see Table 1. The comparison is performed on the basis of (i) the computed pressure profile along the wall in the plane of symmetry, see Fig. 13, and (ii) the computed field of heat release rate (HRR) superimposed on density gradient, see Fig. 14. Concerning the latter, the corresponding quantities are integrated along the transverse direction in order to favor the comparison with experimental visualizations presented in section II. It should be recalled that, for this specific combustion mode, the upper and lower flames are not correlated, and this feature cannot be recovered from the present set of steady-state RANS simulations of half the geometry. Indeed, only the lowest part of the combustion chamber has been computed before mirroring the reactive flowfield, which introduces an artificial correlation between the top and the bottom parts of the visualization.

The global flow features, as revealed by both approaches, i.e., including roughness effects or not, are rather similar. First, in both cases, the impact of the injection is visible in the vicinity of abscissa x = 200 mm. The bow shock formation and its successive reflections on the wall at abscissas approximately equal to x = 240 mm and x = 280 mm are quite well delineated, as shown in Fig. 14. As a consequence of combustion development and mesh coarsening, the other reflections, which take place farther downstream, are more

difficult to detect. These reflections are materialized by the two pressure peaks right downstream of the injection, which are clearly visible in Fig. 13. Following these two pressure peaks, there is a global increase of the pressure level that is induced by the combustion heat release, see also Fig. 14. The combustion starts in the direct vicinity of the walls, extends progressively beyond this region and develops in the core flow. The maximum heat release rate is associated to the local maximum of the pressure observed between x = 350 mm and x = 400 mm. Downstream of these maxima, the computed pressure level decreases with an almost constant slope whereas experimental data exhibit a pressure plateau for 400 mm $< x <$ 600 mm. It should be acknowledged that the occurrence of this plateau would deserve further attention. Because of the diverging section of the combustion chamber in this part of the geometry, some flow separation may occur, which would trigger boundary layer thickening downstream of abscissa x = 400 mm. Another possible explanation may lie in the use of the roughness model. Such models have been indeed developed without any special consideration of a possible adverse pressure gradient and may therefore be unsuited to configurations featuring significant flow acceleration such as the one observed in the diverging section of the combustor. Finally, at the abscissa x = 600 mm, the pressure drops because of the increasing divergence angle.

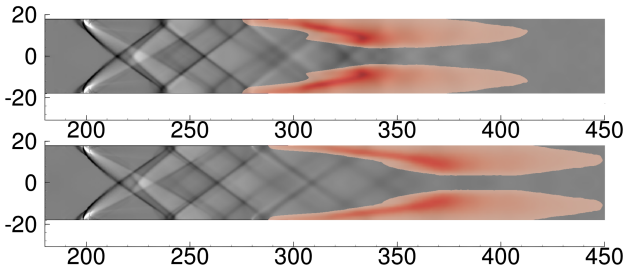

Figure 14 HRR integrated along the width of the combustor superimposed on a Schlieren image. Computations performed with the wall roughness model (top) and without (bottom).

A more detailed inspection of the computational pressure profiles reported in Fig. 13 shows that the level of agreement with experimental data is better when the roughness effects are taken into account. In the non-reacting part of the flow (i.e., for abscissas smaller than 300 mm), the global pressure level is slightly larger, which is an outcome of boundary-layer thickening in the presence of roughness effects. This phenomena also explains that the bow shock reflection occurs at slightly smaller abscissa, i.e., x = 275 mm instead of x = 290 mm for the smooth case. In both cases, combustion starts at the location where the bow

shock impinges the wall, see Fig. 14. This is the preferred location for combustion stabilization since this region features lower velocities and temperature levels larger than those reached in the core of the flow or elsewhere the boundary layer. In the smooth case, because the shock reflection occurs farther downstream, combustion also stabilizes farther downstream. It subsequently spreads over a longer distance. Since the equivalence ratio value is rather small, it is possible to consider that combustion is complete. Therefore, since the available amount of fuel is burnt over a longer distance, the local heat release rate will be weaker and the pressure increase will remain moderate. Despite a slight overestimation of the maximum value, it should be acknowledged that the pressure evolution is better recovered in the presence of roughness effects.

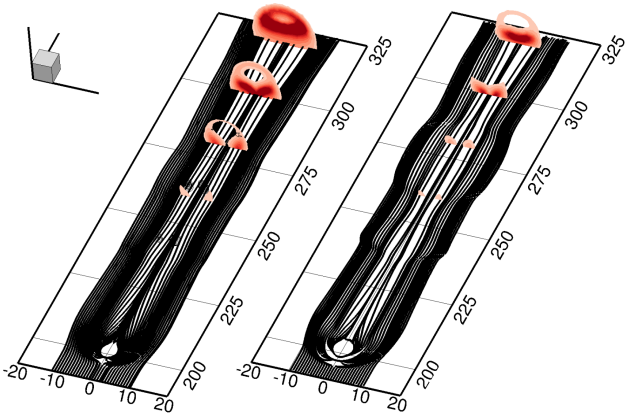

Figure 15 Streamlines in the y = 0.1 mm plane and HRR in the transverse planes x = 260 mm, 280 mm, 300 mm, and 320 mm in the rough (left) and smooth (right) cases.

Figure 15 is now considered to analyze the topology of the reactive flowfield in more details. This figure displays the field of the heat release rate (HRR) in several transverse planes of the computational domain. Skin friction lines are also plotted at the bottom. From these lines, the injector and the imprint of the horseshoe vortex can be clearly delineated. In this respect, it can be noticed that, in comparison to open geometries (e.g., [61]), the presence of the lateral walls tends to restrict the transverse development of this vortex, i.e., its lateral extent. This difference excepted, the reactive flowfield topology of Fig. 15 is rather similar to the one described in the literature, see for instance [62, 63]. In these references, the authors study a transverse reactive jet of hydrogen injected normally to a smooth plate in a supersonic non-vitiated airstream. The

bulk average flow conditions are M = 2.4, P = 0.4 bar and T = 1400 K, which, based on isentropic relations, corresponds approximately to P_t = 6 bar and T_t = 3000 K. The corresponding stagnation temperature level thus appears to be higher than the values considered in the present study. The present computational flow topology appears to be quite similar to the one documented for J = 1.8 in references [62, 63]. The main features of the reactive flowfield are indeed recovered: (i) ignition occurs far downstream of the injection and rather close to the wall, (ii) the most intense burning region remains close to the wall, (iii) shear layer ignition is rather weak and takes place in the vicinity of the symmetry plane. Similar observations have been reported in reference [64]. Most of these features are indeed visible in Fig. 15 but there is however a slight difference.

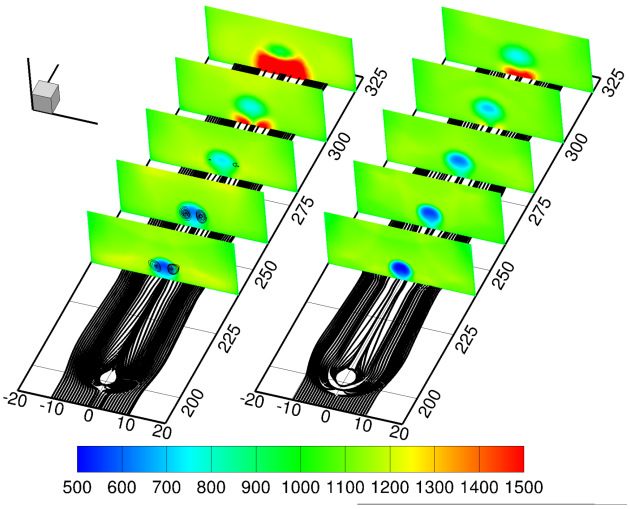

Figure 16 Streamlines in the y = 0.1 mm plane and temperature field in the transverse planes x = 260 mm, 280 mm, 300 mm, and 320 mm in the rough (left) and smooth (right) cases.

Indeed, for x-abscissa larger than 300 mm, chemical reactions tend to develop at a larger distance from the wall, which may be ascribed to the presence of the CTV and enhanced transport. Experimental studies may have missed this special feature because the visualization extent was smaller than the extension of the present computational domain. It is also noteworthy that, since the stagnation temperature level is smaller than the one considered in references [62, 63], the ignition processes taking place in the shear layer remain particularly weak. In view of these differences, which remain quite moderate, it can be stated that the roughness does not seem to alter the canonical reactive flow topology that has been previously observed on a flat plate.

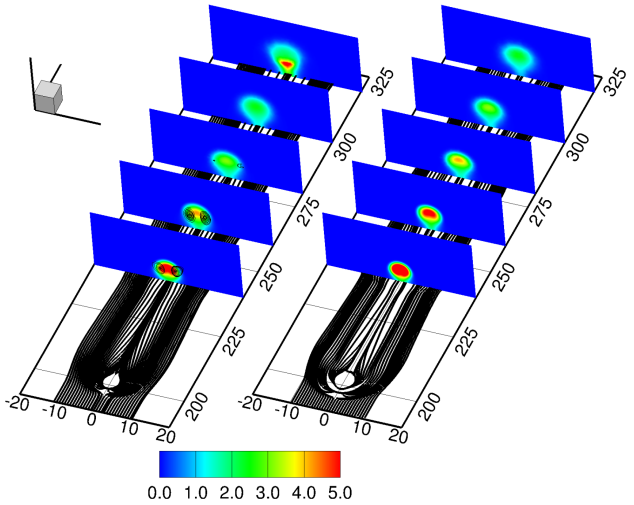

Figure 17 Streamlines in the y = 0.1 mm plane and equivalence ratio field in the transverse planes x = 260 mm, 280 mm, 300 mm, and 320 mm in the rough (left) and smooth (right) cases.

Finally, the possible influence of wall-roughness is assessed by proceeding with a direct comparison between the results issued from smooth and rough computations. As emphasized above, since the interaction between the bow shock reflection and the boundary layer takes place at approximately the same location in the rough-wall or smooth-wall case, combustion stabilizes at approximately the same distance from the hydrogen injector. However, in regard to the combustion development, the influence of wall-roughness appears to be more significant. Indeed, as it can be seen in Figs. 16 and 17, the hydrogen jet heats up and diffuses more rapidly into its environment in the rough case, which is a direct outcome of an increased turbulent viscosity. As a consequence, the combustion development tends to take place at larger distances from the wall and it spreads over a smaller volume.

2. Sudden or sharp (partially choked) combustion mode

The sharp (partially choked) combustion mode, as highlighted from the experiments, is now investigated. In comparison with the supersonic weak combustion mode, it features a higher global equivalence ratio, i.e., 0.145 instead of 0.121, see Table 1. This rather slight increase of the equivalence ratio gives rise to a flow structure that does involve a stronger interaction between shock waves, boundary-layer separation, and combustion.

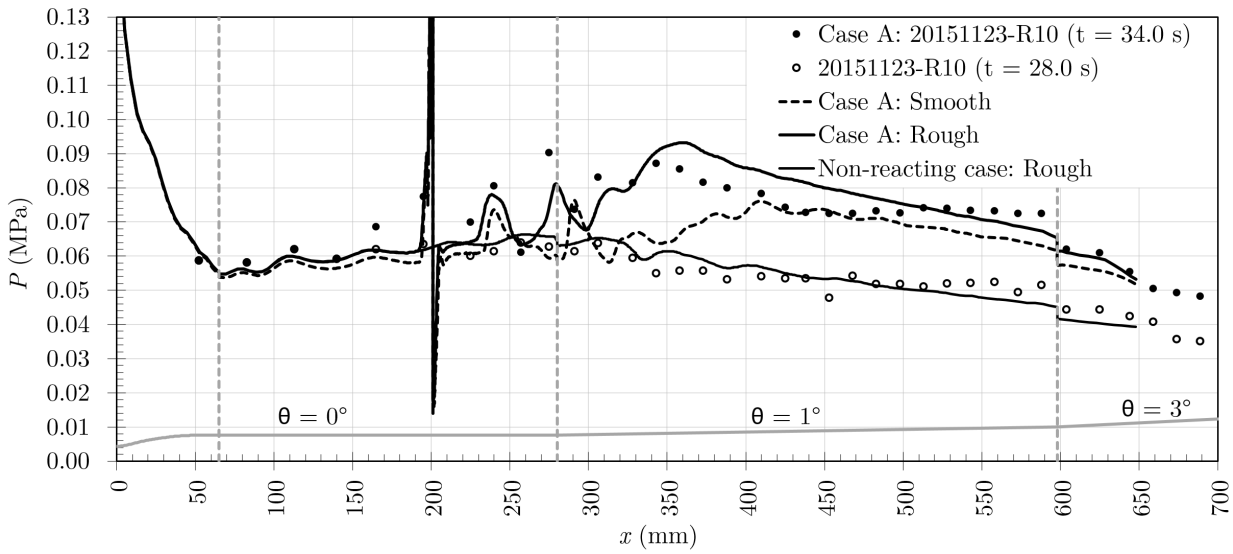

Figure 18 Wall pressure profiles comparison in the plane of symmetry.

The dynamic that leads to the formation of this structure is not studied herein and the objective of this section is, as in supersonic weak combustion case, to assess the possible influence of the wall-roughness on the simulation results once the steady-state is reached.

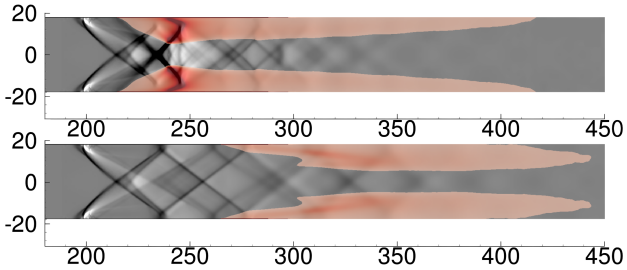

Figure 19 HRR integrated along the width of the combustor superimposed on a Schlieren image. Computations performed with the wall roughness model (top) and without (bottom).

Simulations results are again compared to experiments in terms of (i) pressure longitudinal profiles measured along the wall in the plane of symmetry, see Fig. 18, and (ii) HRR superimposed on density gradient, see Fig. 19. For the smooth-wall simulation, the reactive flowfield topology and the shape of the pressure distribution remain similar to their counterparts obtained for the supersonic weak combustion mode [62, 63]. Smooth-wall results are thus found unable to reproduce properly experimental results, see Fig. 18. However,

by taking into account wall-roughness, the differences observed between the two combustion modes are recovered. Accounting for wall-roughness, the pressure peak observed just downstream of the fuel injection is well recovered by the simulation together with a satisfactory slope of the pressure decrease observed for abscissas $x < 400$ mm. The corresponding pressure peak corresponds to the cross-shaped compressible structure that is identified in both numerical and experimental Schlieren visualizations.

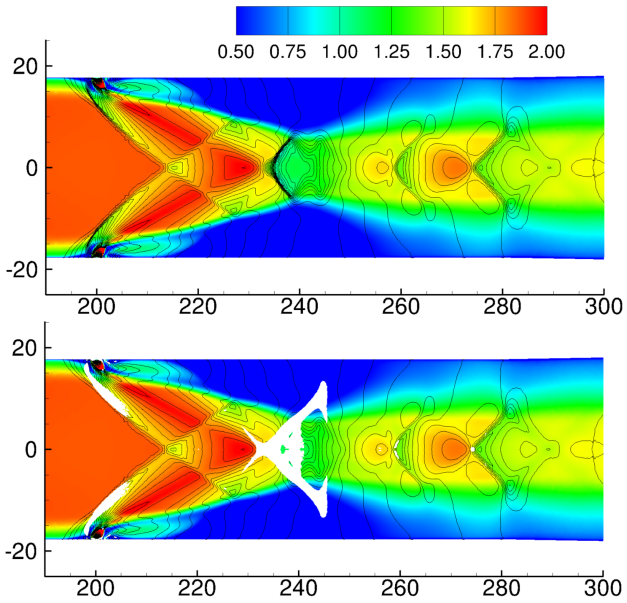

Figure 20 Mach number contours and pressure iso-lines in the plane of symmetry (top). Idem with the projection of an iso-surface of density gradient $\partial\rho/\partial x = 60$ kg m^{-4} (bottom).

The visualisation of this cross-shaped compressible structure, which results from the integration across the transverse direction, is presented in Fig. 20. On the top of this figure, Mach number contours and pressure iso-lines are reported in the plane of symmetry. Upper and lower injections are visible at $x = 200$ mm. Mach numbers and pressure distributions reveal a shock structure that is somewhat similar to a shock train, with series of compressions and expansions in the core flow, bounded by shock waves that interact with a boundary layer subject to separation [65]. Nevertheless, the shock located at $x = 240$ mm displays a more complex shape, as it can be seen on the bottom of Fig. 20, than the one issued from a shock train developping in a constant section duct. In this figure, this shock is marked by an iso-surface of density gradient, calculated in the whole domain and projected onto the plane of symmetry. Figure 21 (bottom) provides a complementary

three-dimensional view of this shock structure. From these two figures, it can be seen that (i) it is highly three-dimensional, and (ii) once projected on the symmetry plane, the cross-shaped structure of Fig. 19 is partially recovered.

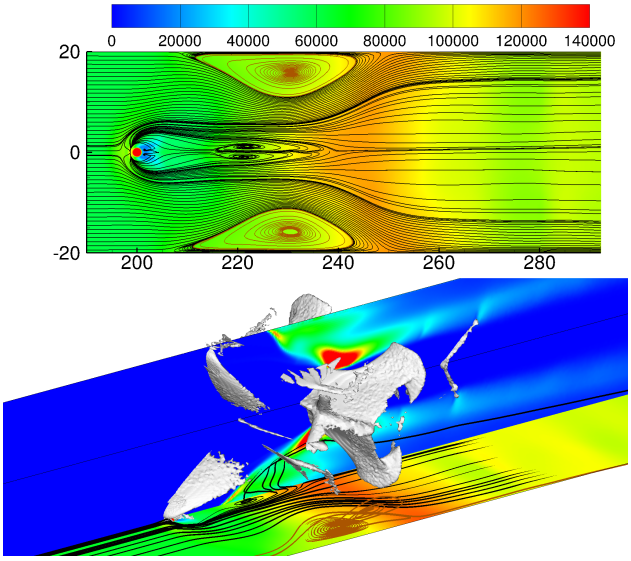

Figure 21 Pressure field and streamlines in the plane $y = 0.1$ mm (top). Same pressure field with HRR in the plane of symmetry, volumic streamlines and iso-surface $\partial\rho/\partial x = 60$ kg m^{-4} (bottom).

The cross shaped shock is delinated by two types of massive boundary layer separation. The first one is marked with the two foci of separation visible at the top of Fig. 21, close to the symmetry plane and for abscissa such that 220 mm $< x <$ 230 mm. The second one is put into evidence with the brown lines at the corner of the chamber (on the top figure). These two types of boundary-layer separation are associated to the adverse pressure gradient induced by the cross-shaped shock structure and combustion.

The two foci of separation close to the symmetry plane reveal vortices with the axis normal to the wall. These vortices eject low momentum fluid into the core flow and then provide favorable conditions for ignition, see the HRR contours in the symmetry plane at the bottom of Fig. 21. Combustion processes appear to be quite intense at the cross-shaped shock location.

From these simulations, it is then confirmed that these three phenomena (i.e., combustion, shock and separation) are more strongly intertwinned in this second sharp combustion mode. As it was mentioned

above, this scenario can then be termed *partially choked* since supersonic flow coexists with large subsonic flow regions. Wall roughness can take part in the choking process in two ways: (i) by thickening the boundary layer and, above all, (ii) by enhancing turbulent mixing and combustion. These two phenomena lead to an increased pressure gradient along the combustor, which promotes thermal choking.

The following conclusions can be drawn from the reactive flow simulations. For the smallest value of the equivalence ratio ER=0.121 (case A), the development of the JISCF in reactive conditions is quite similar to the one previously documented in the literature: there is no significant modification induced by the wall confinement. This is in sharp contrast with case B. In the corresponding conditions, which are associated to a higher value of the ER, the reactive and compressible flow topology changes dramatically compared to case A. As stated in the introduction, the increase in ER favors the occurrence of thermal chocking because of (i) a larger added mass and (ii) an increased heat release in comparison to case A. Thus, the resulting combustion-induced pressure gradient is larger than the one observed in case A. This leads to boundary layer separation and to the formation of the cross-shaped shock structure. This remarkable change in flow topology is related to the wall confinement and, as a consequence, the formation of this compressible flow structure is sensitive to the description of the wall-bounded flow. Thus, roughness, through its influence on the boundary layer development, plays a role in flow conditions relevant to case B. Especially, it may influence the occurrence of thermal chocking, which is of primary interest for scramjet design. This is confirmed by the present set of computations: the consideration of roughness is found to be necessary to reproduce the birth the cross-shaped shock structure.

V. Conclusion

The present study has been devoted to the RANS simulations of the LAPCAT-II dual mode ramjet/scramjet combustor. The thermal barrier coating (TBC) that has been applied to the metallic surfaces of the combustor induces non-negligible wall roughness, which needs to be considered in the numerical simulation. As emphasized in the literature, the resulting increase in wall friction is associated to a shift in the near-wall velocity profile. In the present study, the roughness effect is taken into account within the Menter's k-ω modeling framework. The cornerstone of the proposed approach is to modify the boundary values of k and ω at the wall. This leads to an increased level of turbulent viscosity and a velocity shift that are consistent with experimental results.

The experimental data exhibit two distinct combustion modes. The first mode, referred to as case A in the manuscrit, corresponds to a supersonic weak combustion mode associated to self-ignition processes following a

thermal runaway or induction period. It takes place without significant alteration of the compressible flowfield topology. The second mode, referred to as case B in the manuscript, corresponds to a sharp combustion mode, with heat release taking place closer to the injection. It is associated to substantial modifications of the compressible flowfield including large separation regions that are strongly intertwined with the birth of a strong cross-shaped shock structure and chemical reactions. Therefore, this second combustion mode may also be referred to as a sudden partially choked combustion mode.

The simulations results are assessed on the basis of wall pressure profiles measurements and direct visualizations, i.e., Schlieren and OH^* chemiluminescence. Both computed cases A and B display an improved agreement with experimental data, once the roughness influence is taken into account. Especially, the simulations of the supersonic weak combustion mode (case A), which is closer to the classical and documented topology of the burning jet in supersonic crossflow, leads to an intensified combustion in the presence of wall roughness. In the partially choked combustion mode (case B), the consideration of rough walls is found to be necessary to induce the observed modification of the flow topology. In the absence of wall roughness effects, the flow topology indeed remains similar to the weak combustion mode. Finally, the analysis of the computational results suggests that the combustion enhancement, which is observed in the rough case, may be related to the (i) augmented turbulent transport of heat and chemical species and (ii) increased flow contraction induced by thicker boundary layers, which lead to a decreased velocity and increased temperature in the core flow. For the higher value of the equivalence ratio (case B), the level of heat release is sufficiently large to trigger partial thermal choking. At this level, a challenging objective would be to perform unsteady simulations of the same geometry and conditions including again a wall roughness reprensentation. This is the matter of our ongoing work.

Acknowledgments

The present research was conducted within the framework of a PhD grant co-funded by DGA Ministry of Defense (G. Michel, Technical advisor), and ONERA. The research of Vladimir Sabelnikov is supported by a Grant of the Ministry of Education and Science of the Russian Federation (Contract no. 14.G39.31.0001 of 13.02.2017).

References

[1] Beach, H. L., "Supersonic Mixing and Combustion of a Hydrogen Jet in a Coaxial High-Temperature Test Case," *AIAA Paper 72-1179*, 1972. https://doi.org/10.2514/6.1972-1179.

[2] Cheng, T. S., Wehrmeyer, J. A., Pitz, R. W., Jarrett, O., and Northam, G. B., "Raman Measurement of Mixing and Finite-Rate Chemistry in a Supersonic Hydrogen-Air Diffusion Flame," *Combustion and Flame*, Vol. 99, No. 1, 1994, pp. 157 – 173. https://doi.org/10.1016/0010-2180(94)90087-6.

[3] Baurle, R. A., Hsu, A. T., and Hassan, H. A., "Assumed and Evolution Probability Density Functions in Supersonic Turbulent Combustion Calculations," *Journal of Propulsion and Power*, Vol. 11, No. 6, 1995, pp. 1132–1138. https://doi.org/10.2514/3.23951.

[4] Möbus, H., Gerlinger, P., and Brüggemann, D., "Scalar and Joint Scalar-Velocity-Frequency Monte Carlo PDF Simulation of Supersonic Combustion," *Combustion and Flame*, Vol. 132, No. 1-2, 2003, pp. 3–24. https://doi.org/10.1016/S0010-2180(02)00428-5.

[5] Izard, J. F., Lehnasch, G., and Mura, A., "A Lagrangian Model of Combustion in High-Speed Flows: Application to Scramjet Conditions," *Combustion Science and Technology*, Vol. 181, No. 11, 2009, pp. 1372–1396. https://doi.org/10.1080/00102200903181892.

[6] Gomet, L., Robin, V., and Mura, A., "Influence of Residence and Scalar Mixing Time Scales in Non-Premixed Combustion in Supersonic Turbulent Flows," *Combustion Science and Technology*, Vol. 184, No. 10-11, 2012, pp. 1471–1501. https://doi.org/10.1080/00102202.2012.690259.

[7] Boivin, P., Dauptain, A., Jiménez, C., and Cuenot, B., "Simulation of a Supersonic Hydrogen–Air Auto-ignition Stabilized Flame using Reduced Chemistry," *Combustion and Flame*, Vol. 159, No. 4, 2012, pp. 1779–1790. https://doi.org/10.1016/j.combustflame.2011.12.012.

[8] Moule, Y., Sabelnikov, V., and Mura, A., "Highly Resolved Numerical Simulation of Combustion in Supersonic Hydrogen–Zir Coflowing Jets," *Combustion and Flame*, Vol. 161, No. 10, 2014, pp. 2647 – 2668. https://doi.org/10.1016/j.combustflame.2014.04.011.

[9] Bridel-Bertomeu, T., and Boivin, P., "Explicit Chemical Timescale as a Substitute for Tabulated Chemistry in a H2–O2 Turbulent Flame Simulation," *Combustion Science and Technology*, Vol. 187, No. 5, 2015, pp. 739–746. https://doi.org/10.1080/00102202.2014.962134.

[10] Coclite, A., Cutrone, L., Gurtner, M., Palma, P. D., Haidn, O. J., and Pascazio, G., "Computing Supersonic Non-Premixed Turbulent Combustion by a SMLD Flamelet Progress Variable Model," *International Journal of Hydrogen Energy*, Vol. 41, No. 1, 2016, pp. 632–646. https://doi.org/10.1016/j.ijhydene.2015.10.086.

[11] Waidmann, W., Alff, F., Bohm, M., Brummund, U., Clauss, M., and Oschwald, M., "Supersonic Combustion of Hydrogen/Air in a Scramjet Combustion Chamber," *Space Technology*, Vol. 15, No. 6, 1995, pp. 421–429.

[12] Waidmann, W., Brummund, U., and Nuding, J., "Experimental Investigation of Supersonic Ramjet Combustion (Scramjet)," *Transport Phenomena in Combustion*, Vol. 2, 1996, pp. 1473–1484.

[13] Oevermann, M., "Numerical Investigation of Turbulent Hydrogen Combustion in a Scramjet using Flamelet Modeling," *Aerospace Science and Technology*, Vol. 4, No. 7, 2000, pp. 463–480. https://doi.org/10.1016/S1270-9638(00)01070-1.

[14] Wepler, U., and Koschel, W. W., "Numerical Investigation of Turbulent Reacting Flows in a Scramjet Combustor Model," *AIAA Paper 2002- 3572*, 2002. https://doi.org/10.2514/6.2002-3572.

[15] Berglund, M., and Fureby, C., "LES of Supersonic Combustion in a Scramjet Engine Model," *Proceedings of the Combustion Institute*, Vol. 31, No. 2, 2007, pp. 2497–2504. https://doi.org/10.1016/j.proci.2006.07.074.

[16] Mura, A., and Izard, J. F., "Numerical Simulation of Supersonic Nonpremixed Turbulent Combustion in a Scramjet Combustor Model," *Journal of Propulsion and Power*, Vol. 26, No. 4, 2010, pp. 858–868. https://doi.org/10.2514/1.48074.

[17] Cutler, A., Danehy, P. M., Springer, R. R., and DeLoach, D. P., "CARS Thermometry in a Supersonic Combustor for CFD Code Validation," *AIAA Paper 2002-0743*, 2002. https://doi.org/10.2514/6.2002-743.

[18] Smart, M. K., Hass, N. E., and Paull, A., "Flight Data Analysis of the HyShot 2 Scramjet Flight Experiment," *AIAA Journal*, Vol. 44, No. 10, 2006, pp. 2366–2375. https://doi.org/10.2514/1.20661.

[19] Hannemann, K., Karl, S., Schramm, J. M., and Steelant, J., "Methodology of a Combined Ground Based Testing and Numerical Modelling Analysis of Supersonic Combustion Flow Paths," *Shock Waves*, Vol. 20, No. 5, 2010, pp. 353–366. https://doi.org/10.1007/s00193-010-0269-8.

[20] Vincent-Randonnier, A., Moule, Y., and Ferrier, M., "Combustion of Hydrogen in Hot Air Flows within LAPCAT-II Dual Mode Ramjet Combustor at Onera-LAERTE Facility - Experimental and Numerical Investigation," *AIAA Paper 2014-2932*, 2014. https://doi.org/10.2514/6.2014-2932.

[21] Vincent-Randonnier, A., Sabelnikov, V., Ristori, A., Zettervall, N., and Fureby, C., "An Experimental and Computational Study of Hydrogen–Air Combustion in the LAPCAT II Supersonic Combustor," *Proceedings of the Combustion Institute*, Vol. 37, No. 3, 2019, pp. 3703–3711. https://doi.org/10.1016/j.proci.2018.05.127.

[22] Balland, S., and Vincent-Randonnier, A., "Numerical Study of Hydrogen/Air Combustion with CEDRE Code on LAERTE Dual Mode Ramjet Combustion Experiment," *AIAA Paper 2015-3629*, 2015. https://doi.org/10.2514/6.2015-3629.

[23] Aupoix, B., "Roughness Corrections for the k-ω Shear Stress Transport Model: Status and Proposals," *Journal of Fluids Engineering*, Vol. 137, No. 2, 2015, pp. 1–10. https://doi.org/10.1115/1.4028122.

[24] Nikuradse, J., "Law of Flows in Rough Pipes," *NACA TM 1292*, 1937.

[25] Ligrani, P. M., and Moffat, R. J., "Structure of Transitionally Rough and Fully Rough Turbulent Boundary Layers," *Journal of Fluid Mechanics*, Vol. 162, 1986, p. 69–98. https://doi.org/10.1017/S0022112086001933.

[26] Grigson, C., "Drag Losses of New Ships Caused by Hull Finish," *Journal of Ship Research*, Vol. 36, No. 2, 1992, pp. 182–196.

[27] Wilcox, D. C., "Reassessment of the Scale-Determining Equation for Advanced Turbulence Models," *AIAA Journal*, Vol. 26, No. 11, 1988, pp. 1299–1310. https://doi.org/10.2514/3.10041.

[28] Wilcox, D. C., "Formulation of the k-ω Turbulence Model Revisited," *AIAA Journal*, Vol. 46, No. 11, 2008, pp. 2823–2838. https://doi.org/10.2514/1.36541.

[29] Hellsten, A., and Laine, S., "Extension of k-ω Shear-Stress Transport Turbulence Model for Rough-Wall Flows," *AIAA Journal*, Vol. 36, No. 9, 1998, pp. 1728–1729. https://doi.org/10.2514/2.7543.

[30] Knopp, T., Eisfeld, B., and Calvo, J. B., "A New Extension for k-ω Turbulence Models to Account for Wall Roughness," *International Journal of Heat and Fluid Flow*, Vol. 30, No. 1, 2009, pp. 54–65. https://doi.org/10.1016/j.ijheatfluidflow.2008.09.009.

[31] Yang, X. I. A., and Meneveau, C., "Large Eddy Simulations and Parameterisation of Roughness Element Orientation and Flow Direction Effects in Rough Wall Boundary Layers," *Journal of Turbulence*, Vol. 17, No. 11, 2016, pp. 1072–1085. https://doi.org/10.1080/14685248.2016.1215604.

[32] Viti, V., Neel, R., and Schetz, J. A., "Detailed Flow Physics of the Supersonic Jet Interaction Flow Field," *Physics of Fluids*, Vol. 21, No. 4, 2009, pp. 1–17. https://doi.org/10.1063/1.3112736.

[33] Kawai, S., and Lele, S. K., "Large-Eddy Simulation of Jet Mixing in Supersonic Crossflows," *AIAA Journal*, Vol. 48, No. 9, 2010, pp. 2063–2083. https://doi.org/10.2514/1.J050282.

[34] Refloch, A., Courbet, B., , A., Murrone, Villedieu, P., Laurent, C., Gilbank, P., Troyes, J., Tessé, L., Chaineray, G., Dargaud, J.-B., Quémerais, E., and Vuillot, F., "CEDRE Software," *AerospaceLab Journal*, 2011, pp. 1–10.

[35] Scherrer, D., Dessornes, O., Ferrier, M., Vincent-Randonnier, A., Sabel'nikov, V., and Moule, Y., "Research on Supersonic Combustion and Scramjet Combustors at ONERA," *AerospaceLab Journal*, 2016, pp. 1–24. https://doi.org/10.12762/2016.AL11-04.

[36] Toro, E. F., Spruce, M., and Speares, W., "Restoration of the Contact Surface in the HLL-Riemann Solver," *Shock Waves*, Vol. 4, No. 1, 1994, pp. 25–34. https://doi.org/10.1007/BF01414629.

[37] Van Leer, B., "Towards the Ultimate Conservative Difference Scheme. V. A Second-Order Sequel to Godunov's Method," *Journal of Computational Physics*, Vol. 32, No. 1, 1979, pp. 101–136. https://doi.org/10.1016/0021-9991(79)90145-1.

[38] Van Leer, B., "Towards the Ultimate Conservative Difference Scheme. II. Monotonicity and Conservation Combined in a Second-order Scheme," *Journal of Computational Physics*, Vol. 14, No. 4, 1974, pp. 361–370. https://doi.org/10.1016/0021-9991(74)90019-9.

[39] Chedevergne, F., "Advanced Wall Model for Aerothermodynamics," *International Journal of Heat and Fluid Flow*, Vol. 31, No. 5, 2010, pp. 916–924. https://doi.org/10.1016/j.ijheatfluidflow.2010.05.002.

[40] Chedevergne, F., Casalis, G., and Majdalani, J., "Direct Numerical Simulation and Biglobale Stability Investigations of the Gaseous Motion in Solid Rocket Motors," *Journal of Fluid Mechanics*, Vol. 706, 2012, pp. 190–218. https://doi.org/10.1017/jfm.2012.245.

[41] Dorey, L.-H., Bertier, N., Tessé, L., and Dupoirieux, F., "Soot and Radiation Modeling in Laminar Ethylene Flames with Tabulated Detailed Chemistry," *Comptes Rendus Mecanique*, Vol. 339, No. 12, 2011, pp. 756–769. https://doi.org/10.1016/j.crme.2011.09.004.

[42] Sainte-Rose, B., Bertier, N., Deck, S., and Dupoirieux, F., "Numerical Simulations and Physical Analysis of an Overexpanded Reactive Gas Flow in a Planar Nozzle," *Combustion and Flame*, Vol. 159, No. 9, 2012, pp. 2856–2871. https://doi.org/10.1016/j.combustflame.2012.04.001.

[43] Doisneau, F., Laurent, F., Murrone, A., Dupays, J., and Massot, M., "Eulerian Multi-Fluid Models for the Simulation of Dynamics and Coalescence of Particles in Solid Propellant Combustion," *Journal of Computational Physics*, Vol. 234, 2013, pp. 230–262. https://doi.org/10.1016/j.jcp.2012.09.025.

[44] Moule, Y., Sabelnikov, V., Mura, A., and Smart, M., "Computational Fluid Dynamics Investigation of a Mach 12 Scramjet Engine," *Journal of Propulsion and Power*, Vol. 30, No. 2, 2014, pp. 461–473. https://doi.org/10.2514/1.B34992.

[45] Bird, R., Stewart, W., and Lighfoot, E., *Transport Phenomena*, John Wiley & Sons, Inc. (New-York), 2002.

[46] Menter, F., "Two-Equation Eddy-Viscosity Transport Turbulence Model for Engineering Applications," *AIAA Journal*, Vol. 32, No. 8, 1994, pp. 1598–1605. https://doi.org/10.2514/3.12149.

[47] Launder, B., "Heat and Mass Transport," *Topics in Applied Physics*, Vol. 12, 1976, pp. 231–287. https://doi.org/10.1007/978-3-662-22568-4_6.

[48] Bardina, J. E., Huang, P. G., and Coakley, T. J., "Turbulence Modeling Validation, Testing and Development," *NASA TM 110446*, 1997.

[49] Menter, F., Kuntz, M., and Langtry, R., "Ten Years of Industrial Experience with the SST Turbulence Model," *Heat and Mass Transfer*, Vol. 4, 2003.

[50] Vedovoto, J., da Silveira Neto, A., Mura, A., and Figueira da Silva, L., "Application of the Method of Manufactured Solutions to the Verification of a Pressure-Based Finite-Volume Numerical Scheme," *Computers & Fluids*, Vol. 51, No. 1, 2011, pp. 85–99. https://doi.org/10.1016/j.compfluid.2011.07.014.

[51] Martínez Ferrer, P., Buttay, R., Lehnasch, G., and Mura, A., "A Detailed Verification Procedure for Compressible Reactive Multicomponent Navier–Stokes Solvers," *Computers & Fluids*, Vol. 89, 2014, pp. 88–110. https://doi.org/10.1016/j.compfluid.2013.10.014.

[52] Thomas, J., Diskin, B., and Rumsey, C., "Towards Verification of Unstructured-Grid Solvers," *AIAA Journal*, Vol. 46, No. 12, 2008, pp. 3070–3079. https://doi.org/10.2514/1.36655.

[53] Desornes, O., and Scherrer, D., "Tests of the JAPHAR Dual Mode Ramjet Engine," *Aerospace Science and Technology*, Vol. 9, No. 3, 2005, pp. 211–221. https://doi.org/10.1016/j.ast.2005.01.007.

[54] Potturi, A. S., and Edwards, J. R., "Large-Eddy/Reynolds-Averaged Navier-Stokes Simulation of Cavity-Stabilized Ethylene Combustion," *Combustion and Flame*, Vol. 162, No. 4, 2015, pp. 1176–1192. https://doi.org/10.1016/j.combustflame.2014.10.011.

[55] Fulton, J. A., Edwards, J. R., Cutler, A., McDaniel, J., and Goyne, C., "Turbulence/Chemistry Interactions in a Ramp-Stabilized Supersonic Hydrogen-Air Diffusion Flame," *Combustion and Flame*, Vol. 174, 2016, pp. 152–165. https://doi.org/10.1016/j.combustflame.2016.09.017.

[56] Candler, G. V., Cymbalist, N., and Dimotakis, P. E., "Wall-Modeled Large-Eddy Simulation of Autoignition-Dominated Supersonic Combustion," *AIAA Journal*, Vol. 55, No. 7, 2017, pp. 2410–2423. https://doi.org/10.2514/1.J055550.

[57] Jachimowski, C. J., "An Analytical Study of the Hydrogen-Air Reaction Mechanism with Application to Scramjet Combustion," *NASA TP 2791*, 1988.

[58] Aupoix, B., and Spalart, P. R., "Extensions of the Spalart–Allmaras Turbulence Model to Account for Wall Roughness," *International Journal of Heat and Fluid Flow*, Vol. 24, No. 4, 2003, pp. 454 – 462. https://doi.org/10.1016/S0142-727X(03)00043-2.

[59] Lu, F., and Dickmann, D., "Topology of Supersonic Jet Interaction Flowfields at High Pressure Ratios," *13th International Symposium on Flow Visualization*, 2008.

[60] Dickmann, D. A., and Lu, F. K., "Shock/Boundary-Layer Interaction Effects on Transverse Jets in Crossflow over a Flat Plate," *Journal of Spacecraft and Rockets*, Vol. 46, No. 6, 2009, pp. 1132–1141. https://doi.org/10.2514/1.39297.

[61] Techer, A., Moule, Y., Lehnasch, G., and Mura, A., "Mixing of Fuel Jet in Supersonic Crossflow: Estimation of Subgrid-Scale Scalar Fluctuations," *AIAA Journal*, Vol. 56, No. 2, 2018, pp. 465–481. https://doi.org/10.2514/1.J056251.

[62] Gamba, M., Miller, V. A., and Mungal, M. G., "The Reacting Transverse Jet in Supersonic Crossflow: Physics and Properties," *AIAA Paper 2014-3107*, 2014. https://doi.org/10.2514/6.2014-3107.

[63] Gamba, M., and Mungal, M. G., "Ignition, Flame Structure and Near-Wall Burning in Transverse Hydrogen Jets in Supersonic Crossflow," *Journal of Fluid Mechanics*, Vol. 780, 2015, p. 226–273. https://doi.org/10.1017/jfm.2015.454.

[64] Lee, M. P., McMillin, B. K., Palmer, J. L., and Hanson, R. K., "Planar Fluorescence Imaging of a Transverse Jet in a Supersonic Crossflow," *AIAA Journal*, Vol. 8, No. 4, 1992, p. 729–735. https://doi.org/10.2514/3.23542.

[65] Matsuo, K., Miyazato, Y., and Kim, H.-D., "Shock Train and Pseudo-Shock Phenomena in Internal Gas Flows," *Progress in Aerospace Sciences*, Vol. 35, No. 1, 1999, pp. 33–100. https://doi.org/10.1016/S0376-0421(98)00011-6.